Non-Trivial Materials in EM-FDTD

Michael W. Ammann

Department of Physics
Swiss Federal Institute of Technology (ETH)
Zurich

Submitted as Diploma-Thesis to
Prof. W. Fichtner

Carried out under the supervision of
Dr. N. Chavannes
and
S. Schild

At the
Foundation for Research on Information Technologies in Society (IT'IS)
Zurich

Zurich, March 2007

Abstract

Several finite-difference time-domain (FDTD) algorithms using the additional differential equation (ADE) method were analysed and tested in order to solve Maxwell's equations in non-trivial (linear and non-linear dispersive) materials. A novel and efficient algorithm has been derived that allows to simulate electromagnetic wave propagation in non-trivial materials that have an arbitrary number of linear Drude- and Lorentz-poles and exhibit non-linear Kerr-effect and Raman-scattering. The advantage of this new algorithm is its modularity, that is, each dispersion contribution can be computed separately which allows parallelisation. Moreover, it has improved speed compared with other similar algorithms. A concrete example of materials incorporating several non-trivial properties are the so-called double negative materials (DNMs). Such DNMs were analysed in numerical experiments in order to test the new algorithm.

Summary

Emerging applications of photonics in general and of DNMs in particular involve materials having frequency- and intensity dependent polarisations. The goal of this work was to study the feasibility of the simulation of electromagnetic wave propagation in non-trivial (linear and non-linear dispersive) materials with finite-difference time-domain (FDTD). To this end, several algorithms which, allow the simulation of a specific effect based on the additional differential equation (ADE) method, were analysed and tested. Because it is planned to extend the commercial software Semcad X [1] with advanced dispersion models in future projects, it is of particular interest to know their stability conditions, accuracies and computational costs (memory, speed). It has been found that ADE FDTD is also a possible mean of solving problems related to materials with several non-trivial properties as shown by [2]. The problem of this approach [2] is that it is slow and not modular which is desirable for parallelisation.

The outcome of this thesis is the derivation of a novel and efficient ADE FDTD algorithm that allows to simulate electromagnetic wave propagation in materials that have an arbitrary number of linear Drude- and Lorentz-poles and exhibit non-linear Kerr-effect and Raman-scattering. This new algorithm is designated ADM, standing for arbitrary dispersive materials algorithm. The novel approach is based on the introductino of the intensity as a new variable which allows to update the contribution from the Kerr-effect separately. The update equation for the intensity can then be solved by a fixed-point iteration. Stability conditions of ADM and a convergence criteria for the fixed-point iteration were derived analytically.

ADM has the following advantages:

- Material-Models: linear Drude- and Lorentz-polarisation, non-linear Kerr-effect and Raman-scattering

- Improved Speed: faster than any other similar algorithm

- Modularity: each polarisation contribution can be computed separately (allows parallelisation)

An exemplary application are materials incorporating linear and non-linear dispersion like the so-called double negative materials (DNMs). Such DNMs were analysed in numerical experiments in order to test the new algorithm.

Thesis Outline

In **Part I**, the physical principles of electromagnetic fields, of electromagnetic properties of matter and of electromagnetic field-matter interaction are discussed. Section 1, which briefly reviews Maxwell's equations, is followed by a discussion of linear and non-linear dispersion models in section 2. The basic physical concepts and the important equations that describe the Drude-, Lorentz- and Debye-models of matter as well as of the non-linear Kerr-effect and Raman-scattering are introduced. The properties of DNMs, which are artificial materials, is reviewed in section 3. The interaction of electromagnetic waves with DNMs as well as actual experiments and numerical simulations of other research groups are described. The first part is closed by the presentation of results of numerical experiments of DNMs performed with Semcad X.

Part II covers the discussion of FDTD algorithms that allow to simulate non-trivial materials. Section 4 reviews the standard Yee-algorithm which solves Maxwell's equations in trivial materials. In Section 5, the auxiliary differential equation method (ADE-FDTD) is introduced which allows to model non-trivial materials. Several algorithms that cover Drude-, Lorentz-, Debye-materials and their stability conditions and accuracies are derived and discussed. The second part is closed by a review of an ADE-FDTD algorithm that allows to simulate a material with non-linear Kerr-effect, Raman-scattering and Lorentz-dispersion. This algorithm forms the basic concept of the formulation of an advanced algorithm that is able to simulate any combination of dispersive effects.

In **Part III**, a new algorithm which allows to simulate electromagnetic wave propagation in arbitrary dispersive materials (ADM) such as DNMs is derived. The presented algorithm is as accurate as the one derived in Part II but requires significantly less computational time. The derivation of this new algorithm in section 6 is followed by a stability and accuracy analysis of the ADM-algorithm in section 7. Section 8 presents one-dimensional simulations of DNMs and other non-linear materials that demonstrate the quality of the ADM-algorithm and show some special effects that occur in such materials. The work is concluded by section 9 where a short summary recapitulates the thesis and section 10 which describes upcoming projects based on this thesis and discusses further possible extensions of the new algorithm by inclusion of other effects.

Contents

Part I
Electrodynamics of Media

In this introductory part, different material models to describe the interaction of electromagnetic waves with matter are introduced. Main focus is put on non-trivial (linear dispersive or non-linear dispersive) materials. These models will be used afterward to derive a finite-difference time-domain (FDTD) algorithm to solve Maxwell's equations in these materials. Trivial materials are covered by the standard Yee-algorithm and described at length in [3] and will hence not be discussed here.

1 General Inspection of Maxwell's Equations

Maxwell's Equations Classically, i.e. not quantum-mechanically or relativistically, the electromagnetic field is described by Maxwell's equations:

$$\nabla \wedge \mathbf{E} = -\frac{\partial \mathbf{B}}{\partial t} \tag{1.1a}$$

$$\nabla \wedge \mathbf{H} = \frac{\partial \mathbf{D}}{\partial t} + \mathbf{j} \tag{1.1b}$$

$$\nabla \cdot \mathbf{D} = \rho \tag{1.1c}$$

$$\nabla \cdot \mathbf{B} = 0 \tag{1.1d}$$

The electric current density $\mathbf{j}$ is connected to $\mathbf{E}$ via Ohm's law (where valid, i.e. at sufficiently low intensities):

$$\mathbf{j} = \sigma \mathbf{E} \tag{1.2}$$

where σ is the electric conductivity.

The magnetic field $\mathbf{H}$ and the magnetic flux density $\mathbf{B}$ as well as the electric field $\mathbf{E}$ and the electric flux density $\mathbf{D}$ are connected via the following equations:

$$\mathbf{B} = \mu \mathbf{H} \tag{1.3a}$$

$$\mathbf{D} = \epsilon \mathbf{E}. \tag{1.3b}$$

The magnetic permeability μ and the electric permittivity ϵ are in the most general case time-dependent and imaginary second order tensors. Such a permittivity or permeability gives rise to dispersion, absorption and anisotropy. The free space values will be designated with ϵ_0 and μ_0. In this work, only isotropic materials with dispersion and absorption are considered.

Short Excursion on the Fourier Transform and Convolutions Time-dependent functions can be mapped bijectively with the Fourier transform ($\mathcal{F}$) onto functions depending on spectral frequency:

$$\mathcal{F} : f(t) \mapsto \hat{f}(\omega)$$
$$\mathcal{F}^{-1} : \hat{f}(\omega) \mapsto f(t).$$

The $\hat{\ }$ shall be ignored in future notation as it is all well defined by the function's argument. Hence, dispersion will be described by $\epsilon(\omega)$, $\mu(\omega)$ and by the refractive index $n(\omega)$ (see also equation (1.4)). It has to be pointed out that the signs occurring when applying the Fourier transform to partial derivatives depend on the definition of the Fourier transform. Conventionally, the Fourier transform with negative sign will be used:

$$\mathbf{E(t)} = \int \mathbf{E}(\omega)\mathbf{e^{-i\omega t}d}\omega$$

With this definition the following conversion is valid: $\dot{x}(t) \rightarrow -i\omega x(\omega)$.

The convolution of two functions $f(x)$ and $g(x)$ which are defined on $\mathbb{R}^n$ is defined as

$$f(x) * g(x) = \int_{\mathbb{R}^n} f(x-y)g(x)dy$$

If $f(x)$ and $g(x)$ are Riemann-integrable functions on $\mathbb{R}^n$, i.e. if

$$f(x), g(x) \in L^1(\mathbb{R}^n) = \left\{ \text{f measurable} | \int_{\mathbb{R}^n} |f(x)|dx < \infty \right\}$$

then the following holds

i) $f * g \in L^1(\mathbb{R}^n)$
ii) $f * g = g * f$
iii) $f \hat{*} g = (2\pi)^{\frac{n}{2}} \hat{f}\hat{g}$

Point iii) is important for upcoming discussions: the Fourier transform of a convolution of two functions is equal to the product of the two Fourier-transformed functions.

Electromagnetic Wave Propagation The most simple solutions of Maxwell's equations (1.1) are plane waves

$$E(t) \propto e^{-i(\omega t - n\mathbf{k_0} \cdot \mathbf{x})}$$

where $\mathbf{k_0}$ is the free space wave vector and n is the refractive index which is defined as

$$n = \sqrt{\epsilon\mu}. \tag{1.4}$$

Thus, the dielectric constant $\epsilon(\omega)$ and the magnetic permeability $\mu(\omega)$ are fundamental quantities which determine the propagation of electromagnetic waves in matter.

Consider a plane wave $E(t) \propto e^{-i(\omega t - n\mathbf{k_0} \cdot \mathbf{x})}$. The real parts of $\epsilon(\omega)$ and $\mu(\omega)$ are responsible for refraction, the imaginary parts of $\epsilon(\omega)$ and $\mu(\omega)$ result in absorption of the wave. The imaginary parts of $\epsilon(\omega)$ and $\mu(\omega)$ can be ignored for wave-propagation because their contribution is only the diminution of the wave's amplitude, any altering of phase velocity origins from the real parts. Thus, in the following discussion, only purely real $\epsilon(\omega)$ and $\mu(\omega)$ are considered. If both, $\epsilon(\omega)$ and $\mu(\omega)$ change sign, the sign of n remains unchanged. If they have opposite signs, the refractive index becomes imaginary. The dispersion relation of a monochromatic wave, which describes the connection between the wave vector $\mathbf{k}$ and the frequency ω, is:

$$\mathbf{k^2} = \frac{\omega^2}{\mathbf{c^2}}\mathbf{n^2}. \tag{1.5}$$

If n is purely imaginary, the wave will not propagate in the medium but decay exponentially (evanescent waves, compare for example with total internal reflection) because the dispersion relation 1.5 can only be satisfied for imaginary $\mathbf{k}$ (imaginary ω are non-physical). This is the case if only $\epsilon(\omega)$ is negative which is found in an electrical/gaseous plasma like metals at UV- to Optical frequencies or thin wires structures at GHz frequencies. This will be shown in the sections 2.2 and 3.2.1. An imaginary $\mathbf{k}$ results also if only $\mu(\omega)$ is negative which is the case in a 'magnetic plasma' to be found in structured materials which will be shown in section 3.2.2. On the opposite, materials with equal signs in the real parts of $\epsilon(\omega)$ and $\mu(\omega)$ allow propagating waves.

2 Dispersion Models

2.1 Introductionary Remarks

Dispersion is in first order a material property due to which electromagnetic waves with different frequencies propagate at different velocities. This property can also be described by a frequency dependence of the refractive index. As a result in a dispersive material, a light-pulse, which is a large sum (or an Integral) over many single waves of different wavelengths, is broadened because some waves travel at a higher speed than the others. This is why the group velocity, which is given in one dimension by

$$v_g = \frac{\partial \omega}{\partial k} = \left(\frac{\partial k}{\partial \omega}\right)^{-1},\tag{2.1}$$

is altered when the refractive index depends on ω. The relation between k and ω is given by the dispersion relation (1.5) where $n = n(\omega) = \sqrt{\epsilon(\omega)\mu(\omega)}$. At higher orders, the refractive index may also depend on the intensity of the electromagnetic wave.

In the following sections, the properties of the electromagnetic field inside dielectric materials are described more in detail and the dispersion relations are derived. The spectral properties of the permittivity $\epsilon(\omega)$ are connected to the atomistic properties of a material. The linear contributions of a free electron gas and of harmonically bound electrons to the permittivity $\epsilon(\omega)$ are derived. Finally, a brief discussion of the non-linear Kerr- and Raman-effect are provided.

In a dielectric, equations (1.3) can be rewritten as

$$\mathbf{B} = \mu\mathbf{H} = \mu_0(\mathbf{H} + \mathbf{M})\tag{2.2a}$$
$$\mathbf{D} = \epsilon\mathbf{E} = \epsilon_0(\mathbf{E} + \mathbf{P}).\tag{2.2b}$$

Generally, the magnetic polarization $\mathbf{M}$ is negligible, the magnetic susceptibility being small compared to the electric permittivity.

For the components of the electric polarization $\mathbf{P}$ in the frequency domain one can write using the Einstein convention

$$P_i = \epsilon_0 \left(\chi_i^{1j} E_j + \chi_i^{2jk} E_j E_k + \chi_i^{3jkl} E_j E_k E_l + \cdots\right)\tag{2.3}$$

where χ^n are the dielectric susceptibility tensors of order n. In the time domain, the right hand side of equation (2.3) takes the form of a convolutions.

2.2 Linear Dispersion

Ignoring higher order terms in the series on the right hand side of equation (2.3), yields a polarization **P** that depends linearly on **E**. Frequency dependent first order susceptibilities $\chi^1(\omega)$ that relate **E** to **P** give rise to linear dispersion. The term linear refers to the linearity of **P** in **E** and not to frequency dependence of the susceptibility $\chi^1(\omega)$. A more thorough discussion of the basic physical concepts and their contribution to linear dispersion than the one presented next can be found in [4] or [5].

2.2.1 Drude Media

The dielectric behaviour of metals and semi-conductors with high electron concentration as well as of plasmas is determined by the collective excitation of the free charges. The displacement $x(t)$ of the free charges against the ionic trunks results in positively and negatively charged clouds which exert an attractive force on each other. This so-called Drude-model yields the following equation of motion:

$$nm\ddot{x}(t) + \delta_D\dot{x}(t) = neE(t) \tag{2.4}$$

where δ is a damping constant (pole relaxation time), m is the reduced mass, e is the effective charge and n is the charge density. The electric conductivity σ is related to δ_D. To see this, a stationary current, $\dot{j} \propto \ddot{x}(t) = 0$, is assumed for which the following equation is valid:

$$j = en\dot{x}(t) = \frac{n^2e^2}{\delta_D}E(t) = \sigma E(t)$$

Now the Fourier transform of equation (2.4) is taken and solved for $x(\omega)$. For the polarization **P** one finds the following relations

$$P(\omega) = nex(\omega) \tag{2.5}$$

$$= -\frac{\omega_p^2}{\omega^2 + i\omega\frac{\omega_p^2\epsilon_0}{\sigma(\omega)}}E(\omega) \tag{2.6}$$

$$= \epsilon_0\chi_D^1 E(\omega) \tag{2.7}$$

where the first equation is given by definition and the third equation defines the susceptibility χ_D^1 which is the linear contribution of Drude-Oscillators to the polarization. Furthermore, the Drude-pole frequency is introduced as

$$\omega_p^2 = \frac{ne^2}{\epsilon_0 m_e}.$$

Introducing the high frequency limit $\epsilon_\infty = \epsilon(\omega = \infty)$ one obtains as final expression for the permittivity

$$\epsilon(\omega) = \epsilon_\infty - \frac{\omega_p^2}{\omega^2 + i\omega\frac{\omega_p^2\epsilon_0}{\sigma(\omega)}} \tag{2.8}$$

The real and imaginary part of the derived permittivity $\epsilon(\omega)$ are shown in figure 1. It can be readily seen that at low frequencies the permittivity becomes negative and imaginary, i.e. absorption is high for low frequencies. A closer look at the Drude model with focus on the frequency regime of negative permittivity will be taken in section 3.2.1. An illustrative

Figure 1: The graph shows $\epsilon(\omega)$ as a Drude-oscillator with damping (in arbitrary scales). The solid line is the real, the dashed line the imaginary part of $\epsilon(\omega)$

example of a light-pulse traversing a Drude-medium is shown in section 5.1.5.

2.2.2 Lorentz Media

The excitation of a harmonic oscillator is assumed to produce a dipole-moment

$$p(t) = ex(t) \tag{2.9}$$

where $x(t)$ is the amplitude of the excitation. This situation can be found in systems with electrons that are bound harmonically to the atomic trunks, natural frequencies of molecules with dipole-moment or lattice oscillations of ionic crystals.

Consider the equation of motion for a damped harmonic oscillator (in this context one speaks of a Lorentz-oscillator)

$$\ddot{x}(t) + \delta_L \dot{x}(t) = -\omega_0^2 x(t) + \frac{e}{m} E(t) \tag{2.10}$$

where δ_L is a damping constant (which can be calculated quantum-mechanically), ω_0 is the resonance frequency, m is the reduced mass and e is the effective charge of the dipole. Taking the Fourier transform of equation (2.10) yields

$$-\omega^2 x(\omega) - i\omega\delta_L x(\omega) = -\omega_0^2 x(\omega) + \frac{e}{m} E(\omega)$$

which can be readily solved for $x(\omega)$. For the polarization one finds

$$P(\omega) = nex(\omega) \tag{2.11}$$

$$= \frac{\frac{e^2 n}{m}}{\omega_0^2 - \omega^2 - i\omega\delta_L} E(\omega) \tag{2.12}$$

$$= \epsilon_0 \chi_L^1 E(\omega) \tag{2.13}$$

where n is the charge density. Here, χ_L^1 is the linear contribution of Lorentz-oscillators to the polarization.

By introducing the static dielectric constant $\epsilon_s = \epsilon(\omega = 0)$, the high frequency limit ϵ_∞ and $\Delta\epsilon = \epsilon_s - \epsilon_\infty$ the final expression for the permittivity is given by

$$\epsilon(\omega) = \epsilon_\infty + \frac{\Delta\epsilon\omega_0^2}{\omega_0^2 - \omega^2 - i\omega\delta_L}. \tag{2.14}$$

The real and imaginary part of the derived permittivity $\epsilon(\omega)$ are given in figure 2. The real part first increases rapidly when approaching the resonance and then drops well bellow 0 forming a frequency band in which the permittivity is negative before it increases again to $\epsilon_\infty = \epsilon(\omega = \infty)$. The imaginary part has a peak at the resonance giving rise to high absorption. A closer look at the Lorentz model with focus on the frequency regime of negative permittivity can be found in section 3.2.2. An illustrative example of a light-pulse
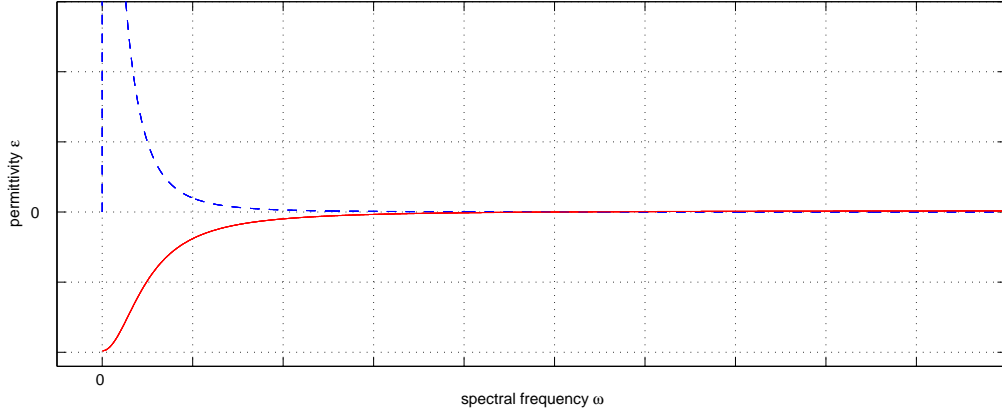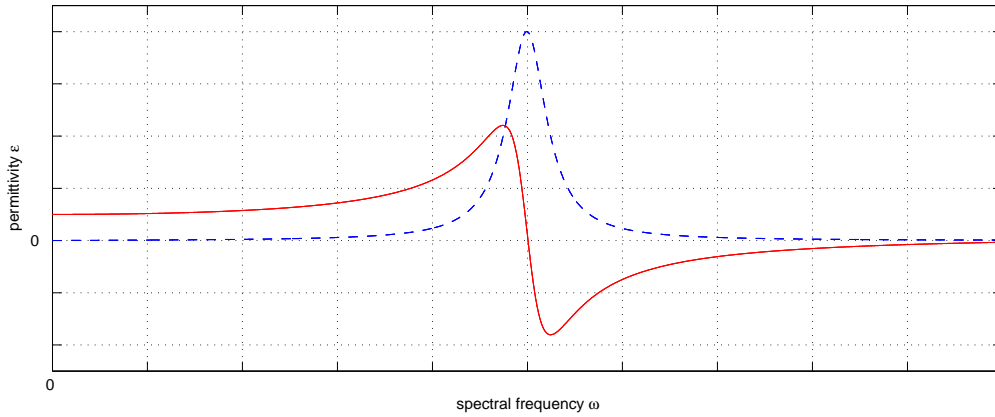

Figure 2: The graph shows $\epsilon(\omega)$ with damping (in arbitrary units). The solid line is the real, the dashed line the imaginary part of $\epsilon(\omega)$

traversing a Lorentz-medium is shown in section 5.2.5.

2.2.3 Debye Media

In the Debye model of a medium, absorption does arise due to dipole relaxation. Assuming a medium of ideal, non-interacting dipoles in a slowly varying electric field, the dipoles' orientation can easily follow the field and the system is always in equilibrium. If the field varies too fast, the dipoles cannot change their orientations fast enough (e.g., due to viscosity) and hence dissipation of the field energy sets in and the field gets absorbed.

The temporal change of the polarization $\mathbf{P}$ due to relaxation of ideal dipoles can be described by the following differential equation

$$\frac{\partial \mathbf{P(t)}}{\partial t} = -\frac{\mathbf{P(t)}}{\tau},$$

where τ is the relaxation time of the dipoles. The stronger the polarization is, the faster is the relaxation. Assuming linear polarization by the electric field $\mathbf{E}$ with an amplitude given by $\Delta \epsilon = \epsilon_s - \epsilon_\infty$ gives

$$\mathbf{P(t)} = \epsilon_0 \mathbf{\Delta \epsilon} \mathbf{E(t)} + \tau \frac{\partial \mathbf{P(t)}}{\partial \mathbf{t}}. \tag{2.15}$$

Taking the Fourier transform of the above equation results in

$$\mathbf{P(\omega)} = \frac{\epsilon_0 \mathbf{\Delta \epsilon}}{1 - \mathbf{i}\omega\tau} \mathbf{E(\omega)} = \epsilon_0 \chi^1_{\mathbf{D_2}} \mathbf{E(\omega)} \tag{2.16}$$

where the linear contribution to the polarization by Debye dipoles $\chi^1_{D_2}$ is recovered. The course of $\epsilon(\omega) = \epsilon_\infty + \chi^1_{D_2}$ in a Debye medium is shown in figure 3. For further details and aspects of non-Debye relaxation reference is made to [6].
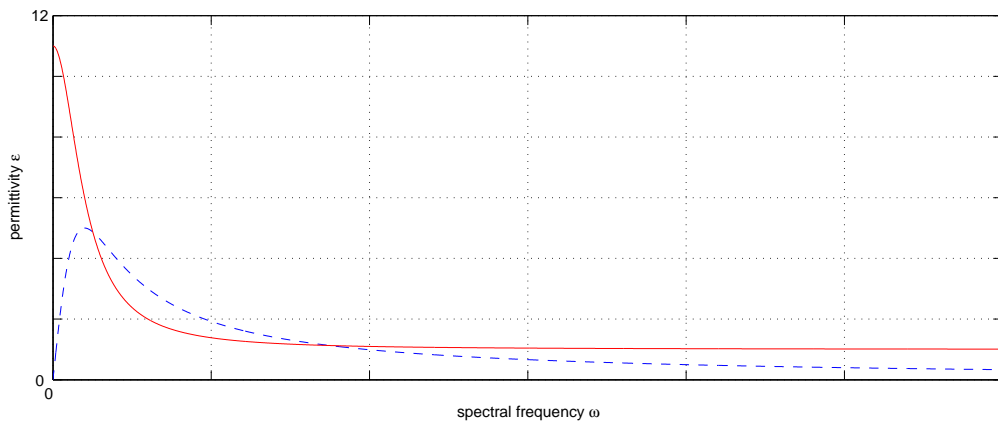

Figure 3: The graph shows $\epsilon(\omega)$ of a Debye medium (in arbitrary scales). The solid line represents the real and the dashed line the imaginary part of $\epsilon(\omega)$.

2.3 Non-linear Effects

The higher order terms on the right hand side of equation (2.3) yield a polarization $\mathbf{P}$ that depends non-linearly on $\mathbf{E}$. As shown below, the second order susceptibility χ^2 cannot exist in an isotropic medium. Therefore, only third order susceptibilities will be discussed.

2.3.1 Second Order Susceptibilities

Isotropy means that the material properties do not depend on the orientation of the coordinate system. Vector-values like the polarization $\mathbf{P}$ and the electric field $\mathbf{E}$ depend on the coordinate system. Let $\mathcal{P}$ be the inversion of space (reflection at the origin). $\mathbf{E}$ and $\mathbf{P}$ transform as follows under $\mathcal{P}$:

$$\mathcal{P}(\mathbf{x}) = -\mathbf{x}$$
$$\mathcal{P}(\mathbf{E}(\mathbf{x})) = \mathbf{E}(-\mathbf{x}) = -\mathbf{E}(\mathbf{x})$$
$$\mathcal{P}(\mathbf{P}(\mathbf{x})) = \mathbf{P}(-\mathbf{x}) = -\mathbf{P}(\mathbf{x})$$

Thus, for the second order susceptibility one finds

$$\mathcal{P}(\mathbf{P_2}(\mathbf{x})) = -\mathbf{P_2}(\mathbf{x}) = \epsilon_0 \chi^2 \mathbf{E}^2$$

which can not be satisfied. Thus, the second order susceptibility in an isotropic material is equal to zero.

2.3.2 Kerr-Effect and Raman-Scattering

In this section, third-order susceptibility contributions to the total polarization will be derived. These susceptibility contributions give rise to an intensity-dependent refractive index. A detailed discussion of these third order non-linear effects would be beyond the scope of this work and the reader is referred to technical literature such as [5] for details. For reasons of brevity, only the derivation of the formulas for the Kerr-effect and Raman-Scattering which will be required for the FDTD formalism (see section 5.5) will be reproduced here following [7] and [2].

In general, the third order non-linear polarization is

$$\mathbf{P(t)} = \epsilon_0 \int \chi^3(\mathbf{t} - \mathbf{t_1}, \mathbf{t} - \mathbf{t_2}, \mathbf{t} - \mathbf{t_3})\mathbf{E(t_1)}\mathbf{E(t_2)}\mathbf{E(t_3)}\mathbf{dt_1}\mathbf{dt_2}\mathbf{dt_3} \tag{2.17}$$

where χ^3 is the third-order susceptibility tensor. For a simple model of the electron response accounting for non-resonant intensity-dependent nonlinear effects, the above equation reduces to the Born-Oppenheimer approximation:

$$\mathbf{P(t)} = \epsilon_0 \chi_0^3 \int \mathbf{g(t - t')}\mathbf{E(t')^2}\mathbf{dt'} \tag{2.18}$$

where $g(t)$ is the normalized causal response function. The induced polarization is assumed to lie in the same direction as the electric field. The non-resonant third-order processes

that will be modeled include phonon interactions and non-resonant electronic effects. The response function can then be described as

$$g(t) = \alpha\delta(t) + (1-\alpha)g_{Raman}(t)$$

where $\alpha \in [0,1]$ represents the relative strengths of the Kerr and Raman polarizations, $\delta(t)$ is a Dirac delta function modeling the instantaneous Kerr non-resonant virtual transitions, and

$$g_{Raman}(t) = \frac{\tau_1^2 + \tau_2^2}{\tau_1^2\tau_2^2}e^{-\frac{t}{\tau_2}}\sin(\frac{t}{\tau_1})U(t)$$

is an approximation of the Raman response function with parameters τ_1 and τ_2 chosen to fit the Raman-gain spectrum, and $U(t)$ is the Heaviside function. $g_{Raman}(t)$ models transient Raman scattering. Effectively, $g_{Raman}(t)$ models a single Lorentzian line centered on the optical phonon frequency $\frac{1}{\tau_1}$ having a bandwidth of $\frac{1}{\tau_2}$, the reciprocal phonon lifetime.

Thus, the polarisation due to Kerr-effect is given by

$$\mathbf{P_{Kerr}(t)} = \epsilon_0\chi_0^3\mathbf{E(t)}\int \alpha\delta(\mathbf{t-t'})|\mathbf{E(t')}|^2\mathbf{dt'}$$
$$= \alpha\epsilon_0\chi_0^3|\mathbf{E(t)}|^2\mathbf{E(t)} \tag{2.19}$$

and the polarisation by Raman-scattering is

$$\mathbf{P_{Raman}(t)} = \epsilon_0\mathbf{E(t)}\left[\chi_{\mathbf{Raman}}^{\mathbf{3}}(\mathbf{t}) * |\mathbf{E(t)}|^{\mathbf{2}}\right] \tag{2.20}$$

where

$$\chi_{Raman}^3(t) = (1-\alpha)\chi_0^3 g_{Raman}(t)$$

The Kerr-effect is simply a frequency-independent, intensity-dependent contribution to the permittivity. Despite that its contribution looks trivial, its effects are very complex. The strength of the Kerr-effect is intensity dependent and depends therefore also on the field amplitude. Thus, different parts of a light-pulse are differently affected by the Kerr-effect. Depending on the sign of the susceptibility χ^3, the Kerr-effect is either focusing, when positive, or defocusing, when negative. In a well balanced case it is possible that the pulse-broadening due to dispersion is neutralised by the Kerr-effect such that the light-pulse retains its shape. Such wave-pulses that retain their shape are called solitons. Some illustrative results of solitons are shown in section 8.2.

3 Double Negative Materials

Materials with a permeability $\mu(\omega)$ and a permittivity $\epsilon(\omega)$ both negative are called double negative materials (DNMs). Such materials have many surprising, counter-intuitive properties that can be derived analytically. As there are no known natural DNMs at any wavelength, they have to be produced artificially. The most important properties of DNMs will be discussed in this section as well as their construction and analysis.

3.1 Requirements and Properties of a DNM

In this section, the work of V. G. Veselago [8] is recapitulated in a nutshell. Despite having no possibility to produce a DNM in 1968, Veselago derived some properties of such a material.

3.1.1 Electromagnetic Field Energy in a Medium

In order to achieve negative $\epsilon(\omega)$ and $\mu(\omega)$ it is essential to have a dispersive medium. To see this, assume first a non-dispersive medium for which the total energy of the electromagnetic field W is given by

$$W = \epsilon \mathbf{E^2} + \mu \mathbf{H^2}. \tag{3.1}$$

Hence, if both $\epsilon(\omega)$ and $\mu(\omega)$ are negative, the total energy of the field is negative. However, if there is dispersion, then the total electromagnetic field energy W is determined by

$$W = \frac{\partial(\epsilon(\omega)\omega)}{\partial\omega}\mathbf{E^2} + \frac{\partial(\mu(\omega)\omega)}{\partial\omega}\mathbf{H^2}. \tag{3.2}$$

In order to achieve a positive total energy W only the partial derivatives in the above equation have to be positive, the values of $\epsilon(\omega)$ and $\mu(\omega)$ can be negative at the same time.

Thus, if a medium shows a certain dispersive behaviour, it is possible to obtain negative $\epsilon(\omega)$ and $\mu(\omega)$ at the same time, which allows propagating waves (see equation (1.5)).

3.1.2 Electromagnetic Wave Propagation in a DNM: Negative Refraction

This section discusses the consequences for the electromagnetic waves entering and traversing a DNM. To this end, first Maxwell's equations are considered

$$\nabla \wedge \mathbf{E} = -\frac{\partial \mathbf{B}}{\partial \mathbf{t}} \tag{3.3a}$$

$$\nabla \wedge \mathbf{H} = \frac{\mathbf{1}}{\mathbf{c}}\frac{\partial \mathbf{D}}{\partial \mathbf{t}} \tag{3.3b}$$

and the constitutive equations

$$\mathbf{B} = \mu\mathbf{H} \tag{3.4a}$$

$$\mathbf{D} = \epsilon\mathbf{E} \tag{3.4b}$$

which reduce for a plane wave into

$$\mathbf{k} \wedge \mathbf{E} = \frac{\omega}{\mathbf{c}} \mu \mathbf{H} \tag{3.5a}$$

$$\mathbf{k} \wedge \mathbf{H} = -\frac{\omega}{\mathbf{c}} \epsilon \mathbf{E}. \tag{3.5b}$$

It is readily seen from the above equations that if $\epsilon(\omega)$ and $\mu(\omega)$ both are positive then $\mathbf{E}$, $\mathbf{H}$ and $\mathbf{k}$ form a right-handed set of vectors and if they are both negative, then they form a left-handed set. That is the reason why DNMs are also often called left-handed media (LHMs) in literature. The energy-flux of an electromagnetic wave is given by Poynting's vector $\mathbf{S}$, which is defined via

$$\mathbf{S} = \frac{\mathbf{1}}{\mathbf{c}} \mathbf{E} \wedge \mathbf{H} \tag{3.6}$$

stating, that $\mathbf{S}$, $\mathbf{E}$ and $\mathbf{H}$ always form a right-handed system. Thus, in a DNM the wave vector $\mathbf{k}$ and Poynting's vector $\mathbf{S}$ are anti-parallel, i.e. point in opposite directions. The point is, that the phase-velocity, which is parallel to $\mathbf{k}$, points in the opposite direction of the energy flux, which is parallel to $\mathbf{S}$. This behaviour is called negative phase velocity and some authors call DNMs also backward-wave materials. It is though not unique to DNMs as it is known to occur in anisotropic media or media with anomalous dispersion (see also [9]).

The most interesting feature of DNMs for technical applications is the negative refraction that occurs in such media. An incident wave on a interface of two media undergoes refraction. While the strength (angle) of the refraction depends on the absolute values of μ and ϵ, the sign of the refraction (positive or negative) depends on the sign of the refraction angle ϕ_2 which again depends on the signs of μ and ϵ.

Consider the boundary conditions at the interface of two media $i = 1, 2$:

$$E_{t_1} = E_{t_2} \tag{3.7a}$$

$$\epsilon_1 E_{n_1} = \epsilon_2 E_{n_2} \tag{3.7b}$$

$$H_{t_1} = H_{t_2} \tag{3.7c}$$

$$\mu_1 H_{n_1} = \mu_2 H_{n_2} \tag{3.7d}$$

where E_{t_i} and H_{t_i} are the electric and magnetic field components parallel to the interface in medium i and E_{n_i} and H_{n_i} are the electric and magnetic field components normal to the interface in medium i. The directions of the parallel components of the electromagnetic field are independent of the handedness of the media. But if the handedness of the two media is not equal, then the normal components have to change sign in order to satisfy the above equations. In fact, this change of sign of the normal field components results in a change of sign of the refractive index of the DNM, i.e. the refractive index n of a DNM is negative.

Despite this change of signs, Snell's law is still valid as $\sin(.)$ is an odd function. Assuming $\phi_2 \in \left[-\frac{\pi}{2}, 0\right]$, the following is valid:

$$n_1 \sin(\phi_1) = n_2 \sin(\phi_2) = n_2 \sin(-|\phi_2|) = -|n_2| \sin(|\phi_2|). \tag{3.8}$$

In that sense, there are two equivalent interpretations available:

1. Snell's law remains unchanged if the refractive index n_2 and the refractive angle ϕ_2 change sign simultaneously. Hence, negative refraction is generally allowed by Snell's law.

2. If there is a negative refractive index n_2, then there has to be negative refraction (negative refraction angle ϕ_2) in order to comply with Snell's law and vice versa.

Again, it has to be pointed out, that negative refraction is not unique to DNMs as it is known to occur also in anisotropic media. The difference of DNMs and anisotropic media that show negative refraction is, that in DNMs the phase vector $\mathbf{k}$ points exactly into the opposite direction of Poynting's vector $\mathbf{S}$ while in anisotropic media $\mathbf{k}$ and $\mathbf{S}$ are not parallel nor anti-parallel.

3.2 Making a DNM

DNMs do not exist in nature and have hence to be synthesised. To create a DNM, the artificial material not only requires dispersive $\epsilon(\omega)$ and $\mu(\omega)$ with frequency bands at which they become negative, these frequency bands also need to overlap.

One can create a DNM by implementing metallic structures into the material. All these artificially created materials that contain micro- or even nano-structures are summarised by the term metamaterials. The structures have to react to electromagnetic waves in a certain manner resulting in an effective negative $\epsilon(\omega)$ and $\mu(\omega)$. As diffraction and refraction of the traversing wave at structures inside the material are undesired, the structures have to be much smaller than the probing wavelength. It is technically desirable to have such materials in the optical, infrared and microwave regimes. Hence, the structures have to be very small (down to few 100 nm). This is also the reason why the first DNMs were obtained at microwave wavelengths.

In the following sections, the underlying structures inside a DNM and their characteristics are introduced. To this end, the important results of Pendry's basic papers of the years 1996 [10] and 1999 [11] will be recapitulated in brief.

3.2.1 Making Negative Permittivity

In this section, Pendry's paper [10] is summarized. An extended calculation of the Drude-oscillator model was provided in section 2.2.1.

It is known that metals whose permittivity $\epsilon(\omega)$ is dominated by the plasma-like response of the free electron gas have negative permittivity $\epsilon(\omega)$ in the optical and near ultraviolet (NUV) bands. This behaviour originates in the presence of so-called plasmons, a collective oscillation of the electron-density. Below the optical frequency band, dissipation destroys the plasmons and typical Drude behaviour sets in.

A displacement of the electron gas inside a metal results in a excess of positive charge from the atomic nuclei. These two charge clouds exert a restoring force on each other resulting in harmonic oscillation at the plasma frequency

$$\omega_p^2 = \frac{ne^2}{\epsilon_0 m_e}$$

where n is the electron density and m_e the electron mass. To have plasmons also present at lower frequencies than they occur in natural materials, their oscillation frequency has to be decreased to the desired one, i.e. the density n has to be decreased and the effective electron mass m_{eff} has to be increased.

The effect of these plasmons on the permittivity is described by a Drude-oscillator model (section 2.2.1):

$$\epsilon(\omega) = 1 - \frac{\omega_p^2}{\omega(\omega + i\delta)} \tag{3.9}$$

where δ is a damping parameter characterising dissipation of the plasmon's energy into the system. The characteristics of the real (solid line) and imaginary (dashed line) parts of $\epsilon_{eff}(\omega)$ are shown in figure 1.

From equation (3.9) and the above graphs one can see, that the real part of $\epsilon(\omega)$ is negative when $\omega < \omega_p$ and the imaginary part becomes dominant when $\omega \ll \frac{\delta}{\omega_p^2}$.

In metals, the electromagnetic response in the optical and NUV bands is determined by the negative ϵ whilst at lower frequencies, i.e. below near infrared (NIR), the dielectric function becomes essentially imaginary and dissipation dominates.

Again, decreasing ω_p extends the regime of negative $\epsilon(\omega)$ with negligible dissipation. Considering the material as a composite of lattice cells containing any arbitrary structure, the main idea is, that an effective permittivity of the material $\epsilon_{eff}(\omega)$ can be defined by averaging fields over one of these lattice cells (details see [11]). Thus, to apply this effective permittivity concept, it is important that the lattice cells are much smaller than the traversing wavelength such that the wave does not see the cell's structure but only its averaged response. The effective permittivity ϵ_{eff} is then defined via the fields that are averaged over one lattice cell as:

$$\mathbf{D_{ave}} = \epsilon_{\mathbf{eff}}\epsilon_0\mathbf{E_{ave}} \tag{3.10}$$

where $\mathbf{D_{ave}}$ is the averaged electric flux density, which is the resulting field from the reaction of lattice cell to the averaged impinging electric field density $\mathbf{E_{ave}}$. With this concept, the structured material can be regarded to be homogeneous. Consider the following arrangement: thin (order μm) metal wires with radius r assembled in a periodic lattice where the wires are separated by a(order mm). The lattice cells are hence of the size a^3 and their inner structure is a thin wire. The use of thin wires instead of a solid block decreases the effective electron density of the material.

Furthermore, the self-induction of the wire structure will act as additional force acting against any restoring force. This effect is included by a new contribution to the effective mass m_{eff} of the electrons in the wires. The final expression for the plasma frequency is then

$$\omega_p^2 = \frac{n_{eff}e^2}{\epsilon_0 m_{eff}} = \frac{2\pi c_0^2}{a^2 \ln(a/r)} \tag{3.11}$$

The overall effect of this wire structure is a decrease of ω_p allowing to tune the real part of $\epsilon(\omega)$ in a broader frequency range. The permittivity provided by such a wire-lattice is generally given by equation (3.9) whose parameters are determined by the geometry of the wire-lattice via equation (3.11).

3.2.2 Making Negative Permeability

In this section Pendry's breakthrough work [11] will be recapitulated briefly. An extended calculation of the Lorentz-oscillator model which emerges here again was provided in section 2.2.2.

Some natural magnetic materials exhibit negative permeability $\mu(\omega)$ up to GHz frequencies. At higher frequencies, any magnetic activity vanishes. Hence, the problem here is to extend the magnetic activity of the material to higher frequencies.

The material is again considered as a composite of lattice cells containing structures. These cells shall be much smaller than the traversing wavelength such that the concept of an effective $\mu(\omega)$ of the material can be applied. The effective permeability μ_{eff} is then defined via the fields that are averaged over one lattice cell as:

$$\mathbf{B_{ave}} = \mu_{\mathbf{eff}}\mu_{\mathbf{0}}\mathbf{H_{ave}} \tag{3.12}$$

where $\mathbf{B_{ave}}$ is the averaged magnetic flux density, which is the resulting field from the reaction of lattice cell to the averaged impinging magnetic field density $\mathbf{H_{ave}}$. While there was a very simple structure for the cells in the effective permittivity case above, there are now aplenty of possible structures that result in a negative permeability. The main idea is that the structures form a LC-circuit in which capacitance C and inductance L balance each other resulting in a resonant form. The most prominent among these resonant structures are the split ring resonator (SRR) whose behaviour results in a effective permeability described by a Lorentz-oscillator:

$$\mu(\omega) = 1 - \frac{F\omega_p^2}{\omega^2 - \omega_p^2 - i\omega\delta} \tag{3.13}$$

where ω_p is the resonance frequency and δ a damping parameter. The constant F and ω_p depend on the geometry of the structure within the lattice cells. The characteristics of the real (solid line) and imaginary (dashed line) parts of $\mu_{eff}(\omega)$ are shown in figure 2.

From equation (3.13) one can see, that the real part of $\mu(\omega)$ is equal to 1 for all $\omega \gg \omega_p$. The course of this permeability is similar to the course of the permittivity shown in figure 2. Approaching ω_p from the low frequency side, $\mu(\omega)$ first increases, is equal to 1 at resonance, becomes less than 1 (or even negative) and approaches again 1. For the imaginary part of $\mu(\omega)$, one can see that it is small except near the resonance. At the resonance it reaches its maximum yielding large absorption. This large absorption near the resonance is quite problematic for the production of transmitting DNMs as the band, where $\mu(\omega)$ is negative, is near the same frequency.

3.3 Non-linear Effects in DNMs

Recent developments in this field pointed out that a non-linear dispersion relation might be useful. Nonlinearities might allow to control the effective parameters of the DNM over a broader frequency spectrum and could be used to produce tunable DNMs. Non-linear effects which give rise to an intensity-dependent permittivity ϵ are readily obtainable by simply using materials that exhibit such a response. Furthermore, the non-linearities can be amplified by inserting a non-linear material in the SRR-gaps because the electric field at these points is extraordinarily strong compared with the field strength of the rest of the cell. It was shown by [12] that there exists non-linearity in the split ring resonators such that the effective magnetic permeability depends on the field intensity. In a very simple approximation for low field-intensities, this intensity-dependence can be described by a Kerr-type non-linear response of the permeability, i.e. [13]:

$$\mu_{eff} \approx \mu + \alpha |\mathbf{H}|^2. \tag{3.14}$$

[12] showed that the non-linearity in μ arises due to a field intensity-dependence of the Lorentz-pole frequency $\omega_p \propto \mathbf{H}^{-2}$. i.e. the resonant frequency of the artificial magnetic structure depends on the amplitude of the external magnetic field which leads in turn to an intensity-dependent permeability $\mu(\mathbf{H}^2, \omega)$.

3.4 Overview on Current Experiments with DNMs

Todays DNM structures are extensively two-dimensional, as three-dimensional, isotropic structures are difficult to produce (so far). Experimental verification of double negativity of a suspected DNM structure is not feasible directly as the phase inside a DNM structure cannot be measured. But the measurement of a transmission band in which a negative refractive index is observed is a strong indication of left-handed behaviour [14] and [15](negative refraction alone is not unique to DNMs [9]). Hence, experiments and simulations are generally performed in parallel to confirm each other mutually. In a 2D-DNM also field scanning at the interior of the DNM can be used to reveal the material's properties [16]. Furthermore, [17] reports the production of an electromagnetic cloak at microwave frequencies.

3.5 Overview on Current FDTD Simulations of DNMs

Finite-Difference Time-Domain (FDTD, see part II) simulations of DNMs can be divided into two groups:

- Structure Simulations

- Material Simulations

In the first group, the two-dimensional DNMs are simulated by implementing the entire resonant structures in three dimensions. This technique is used as a validation of experimental findings as well as a means of engineering DNMs (c.f. [18], [19], [20] and [21]).

In the second group, DNMs are unstructured, homogeneous, isotropic and, in particular, dispersive materials. The present real DNMs are best characterized by a dispersive permittivity $\epsilon(\omega)$ described by Drude-oscillators and a dispersive permeability $\mu(\omega)$ described by Lorentz-oscillators. Realistic models include these two different dispersion relations [22]. For simplicity, also double-Drude and double-Lorentz (i.e. $\epsilon(\omega)$ and $\mu(\omega)$ have the same dispersion relations) DNMs are simulated. A recent development is the use of nonlinear effects originating from SRRs giving rise to new effects such as solitons [23], [24].

Big efforts are made in theoretical studies to understand the physics of DNMs and its applications. Hence, there are many theoretical predictions can be tested. As there are only few DNMs at limited wavelengths available, many experiments are performed numerically. These are done with 2D-FDTD models (c.f. [25] and [26]), while 3D-simulations are just emerging [27]. Especially the possibility of perfect lensing and the associated effects lead to copious theoretical and numerical studies [28] [29].

3.6 DNM Simulations with Semcad X

In the following section, results of simulations of DNMs obtained with the commercial software Semcad X [1] are presented. The DNMs were modelled as structured, three-dimensional media. Besides that it has been shown that Semcad X is able to perform such simulations very efficiently, the concepts of DNMs have been confirmed. These simulations will form a basis for further investigations on DNMs where these results will be compared with those obtained with the new algorithm derived later in this work which can model DNMs as structureless media (see part III). In essence, the findings of [21] and [18] were verified. Despite that the DNMs were modelled fully in three dimensions, the DNM-behaviour occurs only in two dimensions.

In the first numerical experiment, the phase velocity inside the DNM was measured at the frequencies where a negative phase velocity can be expected as proposed in [21] and [18]. To this end, a wave was launched by a dipole onto an array of unit cells which form the DNM (see figure 8). The first investigated DNM consisted of unit cells containing the split ring resonator (SRR) and wire described in [21] and are called therein as 'type 3', the second DNM consisted of those described in [18]. Subsequently, the former DNM structure will be called DNM-1, the latter will be called DNM-2. Both investigated unit cells are shown in the figure 4 and 5 below. The material of the structures in the unit cells was modelled as metal, i.e. as perfect electric conductors (PEC), surrounded by free space.

Figure 4: Configuration of the unit cell of DNM-1 consisting of metallic split ring resonators and wires as described in [21]
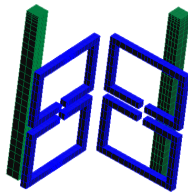

Figure 5: Configuration of the unit cell of DNM-2 consisting of metallic split ring resonators and wires as described in [18].

In order to measure the phase velocity, several edge sensors were set into the unit cells inside the array along one single line. Edge sensors monitor several field entities at one location. Edge sensors do not record the electric field $\mathbf{E}(\mathbf{t})$ with respect to time directly, but they are able to record the induced currents which are simply proportional to $\mathbf{E}(\mathbf{t})$. If the phase velocity is positive, then the electric field in the sensor closer to the wave source always has an advance to the sensors located farther away. If the phase velocity is negative, then the opposite is true, i.e. the recorded phase in the edge sensor farther away from the source precedes the phase recorded at the one closer to the source. With this method, negative phase velocity was confirmed for DNM-1 at 9 GHz and for DNM-2 at 14.5 GHz. The experimental setup is shown in the figures 6, 7 and 8. For DNM-1, a 12x6 array of unit cells was used, for DNM-2 an array of 12x7 (due to reasons of simulation size).

Figure 6: Side on view of the experimental setup for DNM-1. On the very right side of the image is the location of the radiation source, a dipole. The small rectangles within the array are the edge sensors with which the induced current, and thus the electric field $\mathbf{E}$, at these points was measured.
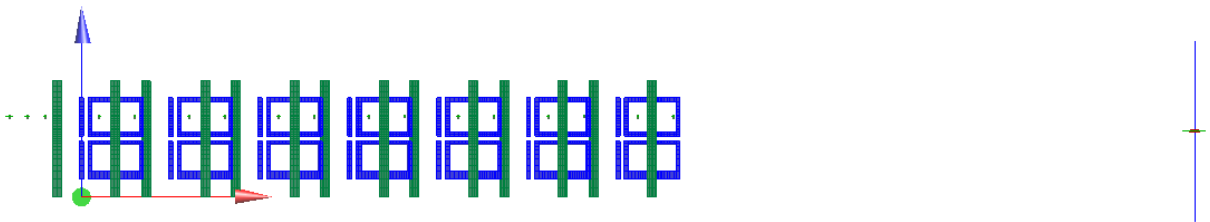
Figure 7: Side on view of the experimental setup for DNM-2. On the very right side of the image is the location of the radiation source, a dipole. The small rectangles within the array are the edge sensors with which the induced current, and thus the electric field $\mathbf{E}$, at these points was measured.
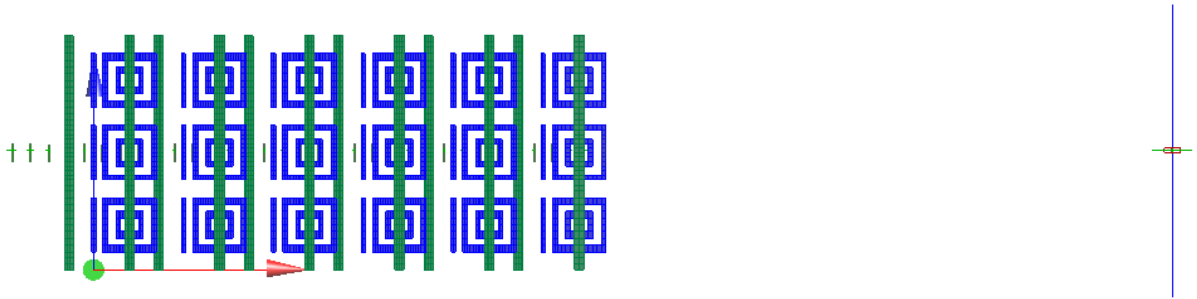
Figure 8: View from above on the experimental setup of DNM-1. On the very right side of the image is the location of the radiation source, a dipole. The small rectangles within the array are the edge sensors with which the induced current, and thus the electric field **E**, at these points was measured. The experimental setup for DNM-2 is similar.
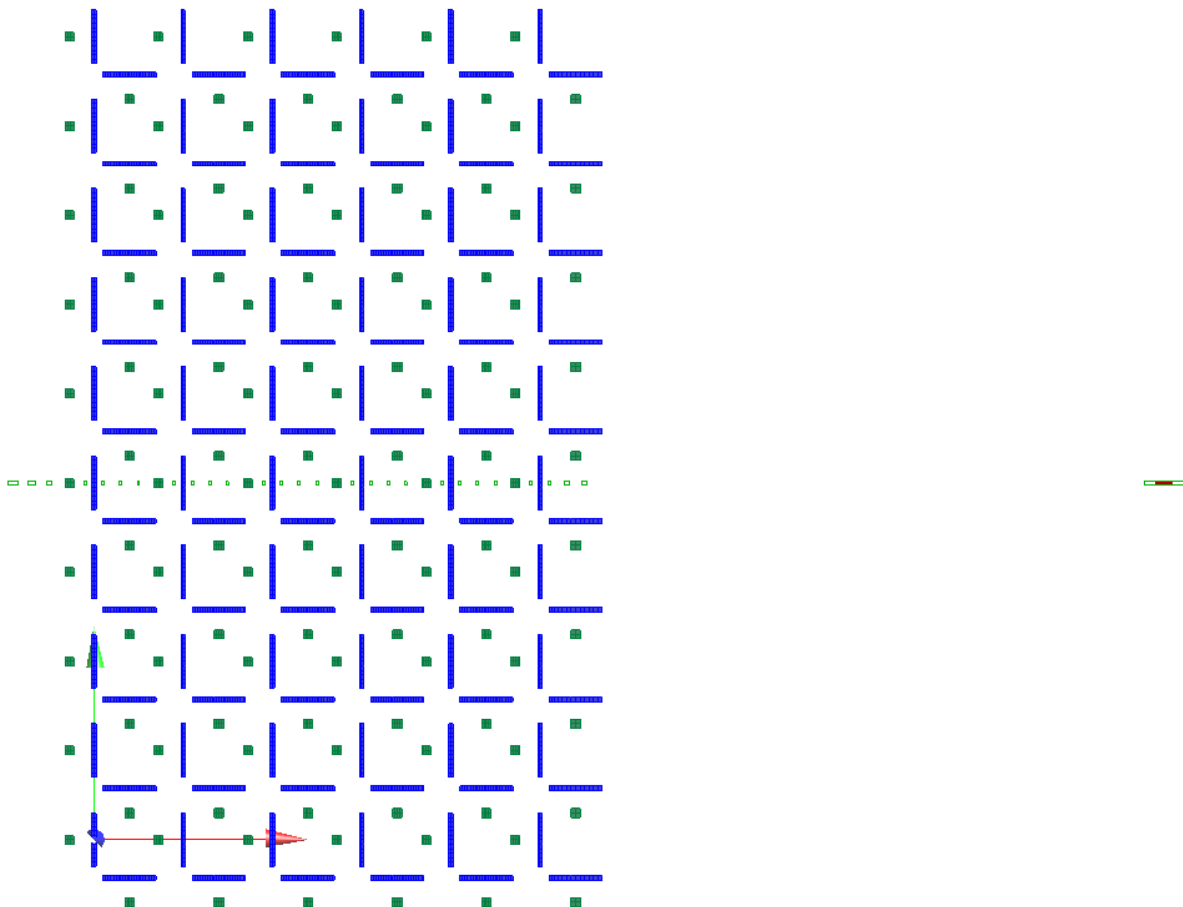
The records of two edge sensors in DNM-1 that are separated by 1 mm are shown in figure 9. The upper figure shows the records of two edge sensors in a unit cell of DNM-1 over 40 periods at 9 GHz. The figure on the lower left shows how the wavefront first encounters the edge sensor closer to the wave source (dashed line), where the induced current is excited somewhat earlier. the lower left figure shows the sensors in steady state, where it can be readily seen, that the phase of the edge sensor farther away from the source (solid line) precedes the phase of the edge sensor closer to the source. This confirms the negative phase velocity at 9 GHz inside DNM-1.

Figure 9: The upper figure shows the records of two edge sensors in a unit cell of DNM-1 over 40 periods at 9 GHz. The figure on the lower left shows how the wavefront first encounters the edge sensor closer to the wave source (dashed line), where the induced current is excited earlier. The figure on the lower left shows the sensors in steady state, where it can be readily seen, that the phase of the edge sensor farther away from the source (solid line) precedes the phase of the edge sensor closer to the source. This confirms the negative phase velocity at 9 GHz.
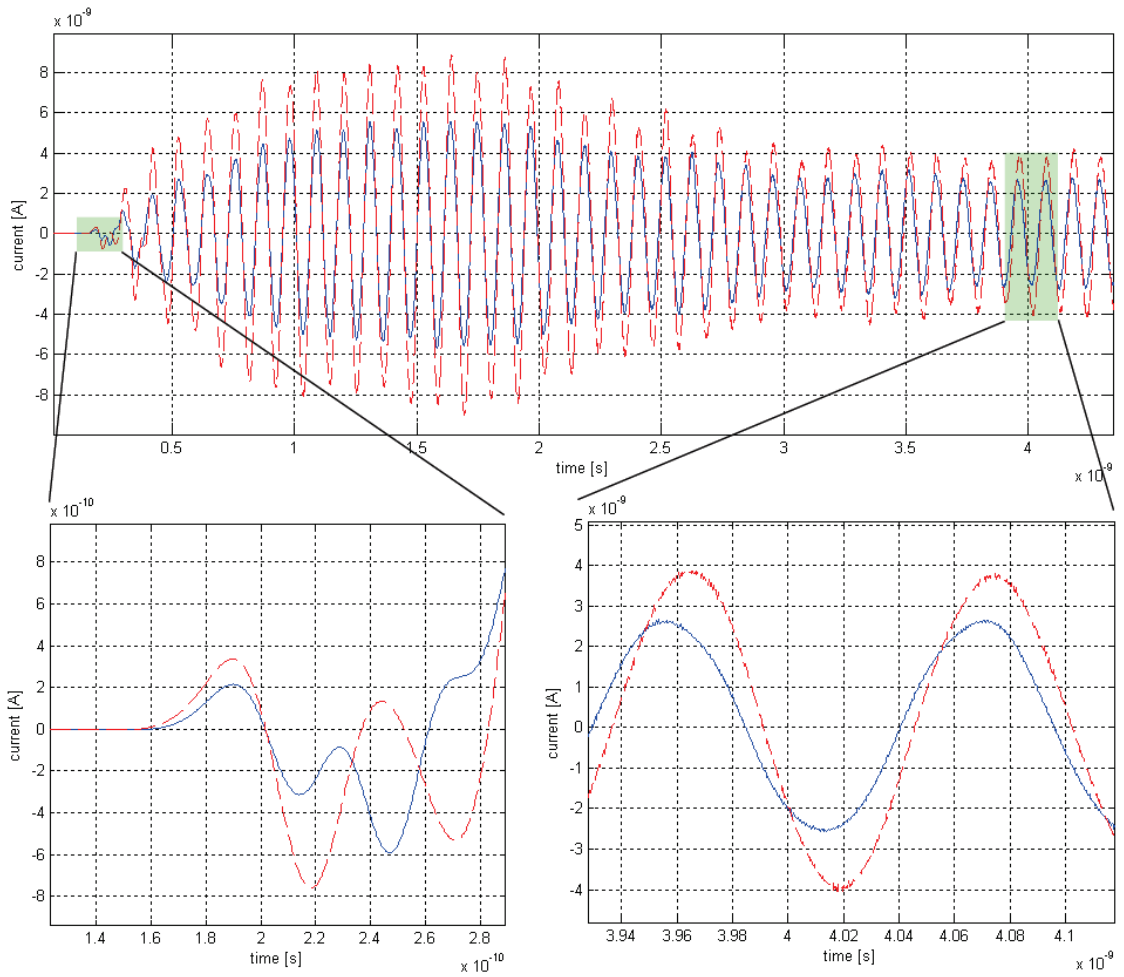
Also the records of two edge sensors in DNM-2 that are separated by 2 mm are shown in figure 10. The upper figure shows the records of two edge sensors in a unit cell of DNM-2 over 40 periods at 14.5 GHz. The figure on the lower left shows that left handed behaviour in DNM-2 sets in immediately. In DNM-2 there is no tune in time to reach left-handed behaviour, which is unlike in DNM-1. The record of the edge sensor farther away from the source (solid line) reveals that the phase at this point is somewhat ahead of the phase measured at the sensor closer to the source (dashed line). These findings confirm the negative phase velocity at 14.5 GHz inside DNM-2.

Figure 10: The upper figure shows the records of two edge sensors in a unit cell of DNM-2 over 40 periods at 14.5 GHz. The figure on the lower left shows that left handed behaviour in DNM-2 sets in immediately. In DNM-2 there is no tune in time to reach left-handed behaviour, which is unlike in DNM-1. The record of the edge sensor farther away from the source (solid line) reveals that the phase at this point is somewhat ahead of the phase measured at the sensor closer to the source (dashed line). These findings confirm the negative phase velocity at 14.5 GHz inside DNM-2.
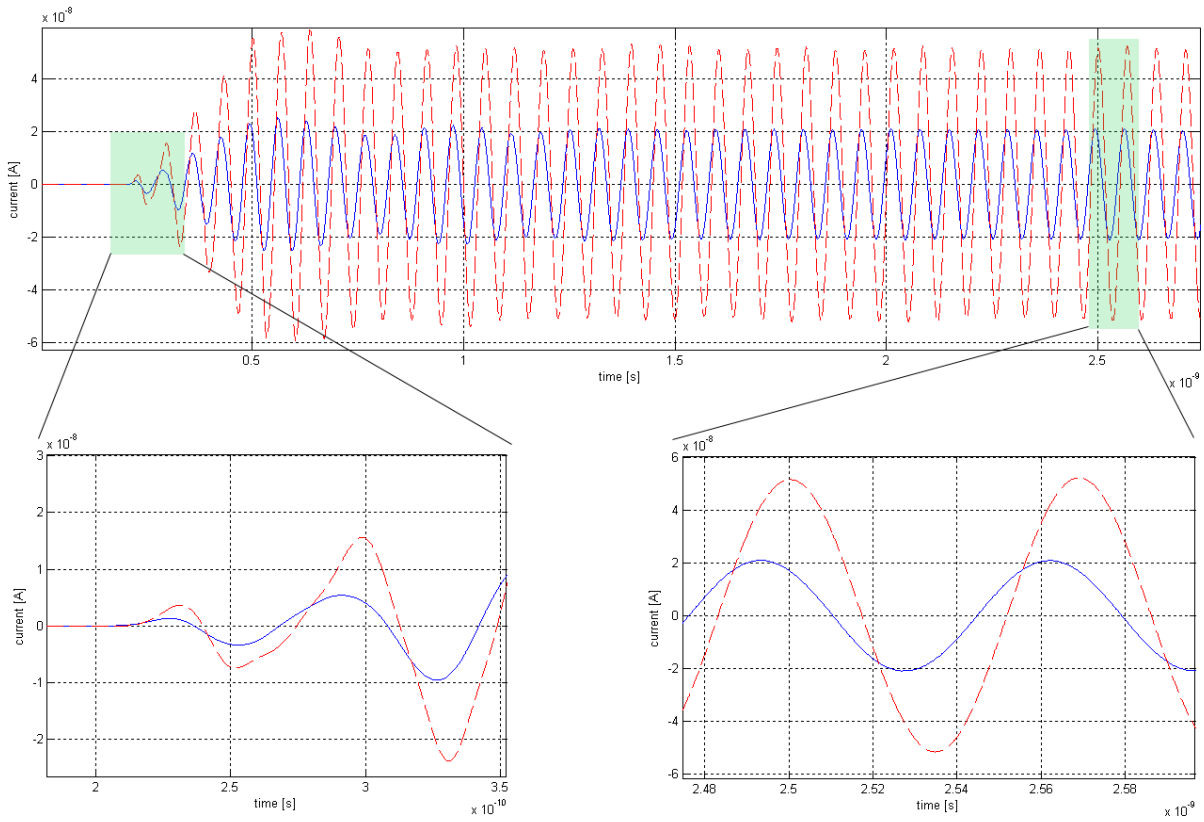
The negative phase velocity is though also directly visible in snapshots of the entire electric field, as well as in animations of the field which are for obvious reasons not shown here. Figure 11 and 12 show such a snapshot of a sliced field view across the entire experiment for DNM-1 and DNM-2 respectively. The thin lines indicate the position of the zero phase. As it can be seen, the deflection of the phasefront inside the DNM is in the opposite direction to the one on the outside, which is a direct manifestation of negative phase velocity.

Figure 11: A snapshot of a sliced field view across the entire experiment using DNM-1. The thin lines indicate the position of the zero phase. As it can be seen, the deflection of the phasefront inside the DNM is in the opposite direction than outside, which is a direct manifestation of negative phase velocity.
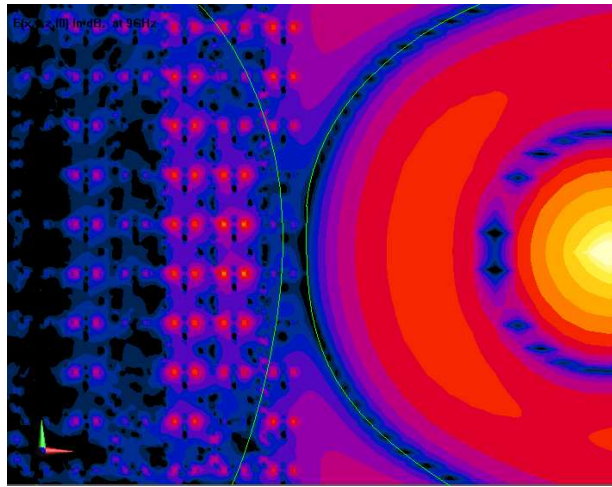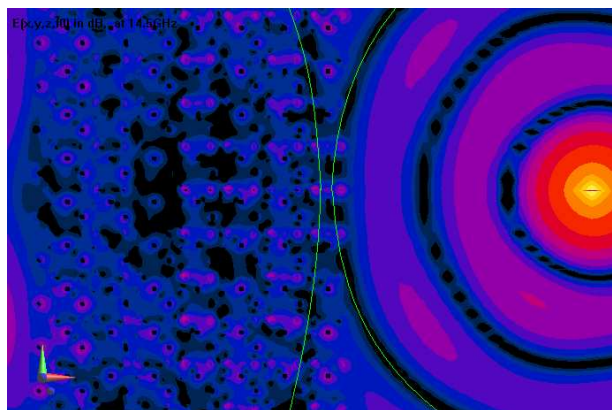

Figure 12: A snapshot of a sliced field view across the entire experiment using DNM-2. The thin lines indicate the position of the zero phase. As it can be seen, the deflection of the phasefront inside the DNM is in the opposite direction than outside, which is a direct manifestation of negative phase velocity.

In a second numerical experiment, the negative refraction has been verified. The electromagnetic wave was launched through a waveguide onto a wedge of DNM-1 of 26.6° and the refraction angle has been measured. The experimental setup is shown figure 13 where the solid line indicates the direction of the refracted beam, and the dot-dashed line the normal to the refraction plane. As it can be readily seen the refraction angle is negative and approximately equal to −5°.
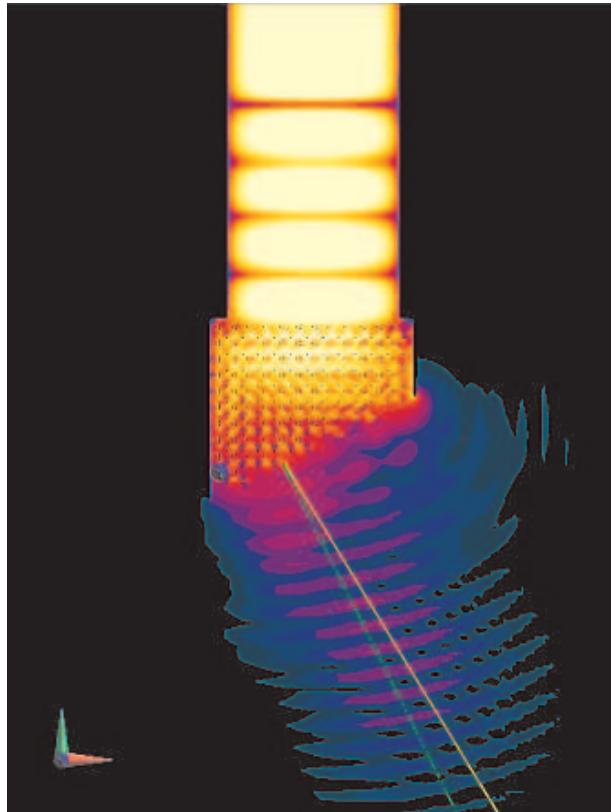
Figure 13: The electromagnetic wave was launched through a waveguide onto a wedge of DNM-1 of 26.6° and the refraction angle has been measured: the solid line indicates the direction of the refracted beam, and the dot-dashed line the normal to the refraction plane. As it can be readily seen the refraction angle is negative and approximately equal to −5°.

Summary of Validation   The findings of [21] and [18] were verified. It has been shown by modelling the metamaterial's structures in three dimensions and performing standard FDTD simulations that for frequencies around 9.5 GHz, DNM-1 exhibits double negative behaviour by measuring negative phase velocity as well as negative refraction. The same is true for DNM-2 at frequencies around 14.5 GHz.

3.7 Summary on DNMs

In the following, the properties of DNMs that were discussed so far are summarised:

1. DNM Characteristics
   - Negative $\mu(\omega)$ and $\epsilon(\omega)$ (both negative allows wave propagation: equations (1.4) and (1.5))
   - Dispersion (field energy (3.2) needs to be positive)
     $\mu(\omega)$ described by Lorentz-oscillator (3.13) (SRR, Swiss rolls)
     $\epsilon(\omega)$ described by Drude-oscillator (3.9) (metal wires)
   - Non-linear effects arise through intensity-dependence of $\mu(\mathbf{H^2}, \omega)$ (3.14)

2. Electromagnetic Waves in a DNM
   - left-handed electromagnetic waves (from Maxwell's equations (3.5))
   - Poynting's vector (3.6) and wave vector point in opposite directions (from Maxwell's equations (3.4), negative phase velocity)
   - Negative refraction (from field continuity across medium-boundaries: equation (3.7))

The discussion about DNMs will be continued in section 8.1 where further numerical DNM-experiments performed by the author with a new algorithm are reviewed. The reader is also referred to that section to see further illustrations of light traversing a DNM.

Part II
The Finite-Difference Time-Domain Method

This section concentrates on the very successful numerical method for the integration of Maxwell's equations in arbitrary structures called the finite-difference time-domain method (FDTD) which bases on the Yee-algorithm [30]. For the description of the basic ideas of FDTD the derivations in [3] are largely followed.

4 Yee-Algorithm

Yee's algorithm which was introduced in 1966 to solve Maxwell's equation (1.1) is very successful as it is very robust. The algorithm solves for both electric and magnetic fields in time and space using the coupled Maxwell's curl equations. The usage of both $\mathbf{E}$ and $\mathbf{H}$ information turns the algorithm particularly robust [3].

The Yee-algorithm centers its $\mathbf{E}$ and $\mathbf{H}$ components in three dimensional space so that every $\mathbf{E}$ component is surrounded by four circulating $\mathbf{H}$ components and every $\mathbf{H}$ component is surrounded by four circulating $\mathbf{E}$ components. Hence, the algorithm simultaneously simulates the pointwise differential form and the macroscopic integral form of Maxwell's equations. The finite-difference expressions for the space derivatives used in the curl operators are central-difference in nature and second-order accurate. Continuity of tangential $\mathbf{E}$ and $\mathbf{H}$ is naturally maintained across an interface of dissimilar materials if the interface is parallel to one of the lattice coordinate axes. The Yee-mesh is divergence-free with respect to its $\mathbf{E}$ and $\mathbf{H}$ fields in absence of free electric and magnetic charge, i.e. it satisfies naturally the Gauss laws. The finite-difference expressions for the time derivatives are central-difference in nature and second-order accurate. The centering of $\mathbf{E}$ and $\mathbf{H}$ components in time results in a leapfrog time stepping scheme. The Yee-algorithm is explicitly given by the following update equations which have to be solved for any grid point inside the Yee-mesh at every time step n:

$$\mathbf{H^{n+\frac{1}{2}}} = C_1^{\mu}\mathbf{H^{n-\frac{1}{2}}} + \mathbf{C_2^{\mu}}\left(\nabla \wedge \mathbf{E^n} - \mathbf{K^{n-\frac{1}{2}}}\right) \tag{4.1a}$$

$$\mathbf{E^{n+1}} = C_1^{\epsilon}\mathbf{E^n} + \mathbf{C_2^{\epsilon}}\left(\nabla \wedge \mathbf{H^{n+\frac{1}{2}}} - \mathbf{J^n}\right) \tag{4.1b}$$

where $\mathbf{J}$ and $\mathbf{K}$ are source currents for the electric and the magnetic field respectively (electric and magnetic currents are included in the equations via conductivities $\sigma^{m,e}$ using

Ohm's law). The update coefficients are given by the following expressions:

$$C_1^{\mu,\epsilon} = \frac{1 - \frac{\sigma^{e,m}\Delta t}{2\epsilon,\mu}}{1 + \frac{\sigma^{e,m}\Delta t}{2\epsilon,\mu}}$$

$$C_2^{\mu,\epsilon} = \frac{\frac{\Delta t}{\epsilon,\mu}}{1 + \frac{\sigma^{e,m}\Delta t}{2\epsilon,\mu}}$$

where either ϵ or μ at the specific grid position has to be chosen. It can be shown analytically, that the Yee-algorithm in one dimension is stable if

$$S = \frac{c_0\Delta t}{\Delta x} \leq 1, \tag{4.2}$$

where S is called the Courant-number. For two and three dimensions, similar stability conditions can be found.

5 Auxiliary Differential Equation Finite-Difference Time-Domain Method

The auxiliary differential equation (ADE) method to model dispersive materials in FDTD utilises time-domain auxiliary differential equations linking polarization and the electric flux density. These equations are time-stepped in synchronism with Maxwell's curl equations, yielding a composite, self-consistent system. ADE methods have second order accuracy. Their time-domain basis makes modeling of arbitrary nonlinear dispersive media particularly attractive. Furthermore, this method bypasses the computation of convolutions which are present when solving equation (2.3) in the time domain. The ADE-FDTD formulation will only be derived for the electric field, but it is analogously applicable to the magnetic field.

5.1 Drude Medium with ADE-FDTD

Two different ADE-FDTD algorithms for Drude dispersive media will be introduced next. The difference lies in the number of stored variables and in accuracy while computational speed is similar.

5.1.1 Formalism with Polarisation

Consider a multiterm Drude dispersive medium having a total of D poles in its susceptibility response. Ampere's law is given by:

$$\nabla \wedge \mathbf{H} = \epsilon_0 \epsilon_\infty \frac{\partial \mathbf{E}}{\partial \mathbf{t}} + \sum_{\mathbf{d=1}}^{\mathbf{D}} \frac{\partial \mathbf{P_d}}{\partial \mathbf{t}} + \sigma \mathbf{E}. \tag{5.1}$$

where $\mathbf{P_d}$ is the polarization associated with the dth Drude pole. The goal of the ADE technique is to develop a simple time-stepping scheme for $\mathbf{P_d}$ that can be updated synchronously with (5.1). Recalling equation (2.4) of the Drude-oscillator one can write in the frequency domain

$$\begin{aligned}\mathbf{P_d}(\omega) &= \epsilon_0 \chi_D^1 E(\omega) \\ &= -\frac{\epsilon_0 \omega_d^2}{\omega^2 + i\omega\delta_d} E(\omega).\end{aligned} \tag{5.2}$$

Multiplication of both sides of the above equation with $(\omega^2 + i\omega\delta_d)$ gives

$$\omega^2 \mathbf{P_d}(\omega) + \mathbf{i}\omega\delta_\mathbf{d}\mathbf{P_d} = -\epsilon_0\omega_\mathbf{d}^2\mathbf{E}$$

Taking the Fourier transform of the above equation yields the desired ADE:

$$\ddot{\mathbf{P}}_d + \delta_d\dot{\mathbf{P}}_d = \epsilon_0\omega_d^2\mathbf{E} \tag{5.3}$$

Applying finite-difference expressions to (5.3) centered at time step n and some algebraic manipulation yields the desired update scheme for $\mathbf{P_p}$:

$$\mathbf{P_d^{n+1}} = \alpha_\mathbf{d}\mathbf{P_d^n} + \beta_\mathbf{d}\mathbf{P^{n-1}} + \gamma_\mathbf{d}\mathbf{E^n} \tag{5.4}$$

with the update coefficients

$$\alpha_d = \frac{4}{\delta_d \Delta t + 2}$$
$$\beta_d = \frac{\delta_d \Delta t - 2}{\delta_d \Delta t + 2}$$
$$\gamma_d = \frac{2\epsilon_0 \Delta t^2 \omega_d^2}{\delta_d \Delta t + 2}$$

The update equation for the electric field can then be derived by evaluating Ampere's law (5.1) at time step $n + \frac{1}{2}$:

$$\mathbf{E^{n+1}} = \mathbf{C_1}\mathbf{E^n} + \mathbf{C_2}\left(\nabla \wedge \mathbf{H^{n+\frac{1}{2}}}\right) - \mathbf{C_3}\sum_{\mathbf{d=1}}^{\mathbf{D}}\left(\mathbf{P_d^{n+1}} - \mathbf{P_d^n}\right) \tag{5.5}$$

with the update coefficients

$$C_1 = \frac{2\epsilon_0\epsilon_\infty - \sigma\Delta}{2\epsilon_0\epsilon_\infty + \sigma\Delta}$$
$$C_2 = \frac{2\Delta t}{2\epsilon_0\epsilon_\infty + \sigma\Delta}$$
$$C_3 = \frac{2}{2\epsilon_0\epsilon_\infty + \sigma\Delta}$$

Thus, the algorithm starts with the electric field update via (5.5), then the polarization currents are updated via (5.4). In the concluding step, the magnetic field is updated via equation (4.1a), which completes the algorithm. We will refer to this algorithm in the rest of this document as $DADE^+$ algorithm. The $+$ indicates that this algorithm is more accurate and needs to store one more variable than the $DADE$ algorithm which will be derived next.

5.1.2 Formalism with Polarisation Current

The same approach as in the previous section is taken again. Thus, consider again a multiterm Drude dispersive medium having a total of D poles in its susceptibility response. One can write Ampere's law also in the following form:

$$\nabla \wedge \mathbf{H} = \epsilon_0\epsilon_\infty\frac{\partial \mathbf{E}}{\partial \mathbf{t}} + \sum_{\mathbf{d=1}}^{\mathbf{D}}\mathbf{J_p} + \sigma\mathbf{E}. \tag{5.6}$$

Here, $\mathbf{J_d}$ is the polarization current associated with the dth Drude pole, i.e. $\mathbf{J} = \dot{\mathbf{P}}$. Using again equation (2.4) of the Drude-oscillator one can write in the frequency domain

$$\mathbf{J_d}(\omega) = -i\omega\epsilon_0\chi_D^1 E(\omega)$$
$$= i\omega\frac{\epsilon_0\omega_d^2}{\omega^2 + i\omega\delta_p}E(\omega). \tag{5.7}$$

Multiplication of both sides of the above equation with $(\omega^2 + i\omega\delta_d)$ gives

$$\omega^2 \mathbf{J_d}(\omega) + \mathbf{i}\omega\delta_\mathbf{d}\mathbf{J_d} = \mathbf{i}\omega\epsilon_\mathbf{0}\omega_\mathbf{d}^\mathbf{2}\mathbf{E}$$

Taking the Fourier transform of the above equation returns it into the time-domain where an integration over time yields the desired ADE:

$$\dot{\mathbf{J}}_d + \delta_d \mathbf{J_d} = \epsilon_\mathbf{0}\omega_\mathbf{d}^\mathbf{2}\mathbf{E} \tag{5.8}$$

Applying finite-difference expressions for the partial derivations to (5.8) and some algebraic manipulation yields the desired update scheme for $\mathbf{J_d}$:

$$\mathbf{J_d^{n+1}} = \alpha_\mathbf{d}\mathbf{J_d^n} + \beta_\mathbf{d}\left(\mathbf{E^{n+1}} - \mathbf{E^n}\right) \tag{5.9}$$

with the update coefficients

$$\alpha_d = \frac{1 - \frac{\delta_d \Delta t}{2}}{1 + \frac{\delta_d \Delta t}{2}}$$

$$\beta_d = \frac{\frac{\omega_d^2 \epsilon_0 \Delta t}{2}}{1 + \frac{\delta_d \Delta t}{2}}$$

The update equation for the electric field can then be derived by evaluating Ampere's law (5.6) at time step $n + \frac{1}{2}$:

$$\mathbf{E^{n+1}} = \mathbf{C_1}\mathbf{E^n} + \mathbf{C_2}\left(\nabla \wedge \mathbf{H^{n+\frac{1}{2}}} - \frac{\mathbf{1}}{\mathbf{2}}\sum_{\mathbf{d=1}}^{\mathbf{D}}\left(\mathbf{1} + \alpha_\mathbf{d}\right)\mathbf{J_p^n}\right) \tag{5.10}$$

with the update coefficients

$$C_1 = \frac{2\epsilon_0\epsilon_\infty - \Delta t \sum_{d=1}^{D}\beta_d - \sigma\Delta t}{2\epsilon_0\epsilon_\infty + \Delta t \sum_{d=1}^{D}\beta_d + \sigma\Delta t}$$

$$C_2 = \frac{2\Delta t}{2\epsilon_0\epsilon_\infty + \Delta t \sum_{d=1}^{D}\beta_d + \sigma\Delta t}$$

Thus, the algorithm starts with the electric field update via (5.10), then the polarization currents are updated via (5.9). In the concluding step, the magnetic field is updated via equation (4.1a), which completes the algorithm. We will refer to this algorithm in the rest of this document as $DADE$ algorithm.

5.1.3 Stability of $DADE^+$ Algorithm

In this section, the stability and phase error of $DADE^+$ will be derived. The used methodology is presented in [3] and [31]. As a result, a stability condition is found which determines how to chose the spatial sampling Δ and the temporal sampling Δt.

An algorithm is stable if it remains bounded for any time, it is unstable if its absolute values grow to ∞. If an algorithm is unstable, the instability often grows exponentially. Apparently, if an algorithm is unstable, the results are wrong. The phase error of the algorithm describes how much faster or slower a numerical wave front is compared with the physical wave front. While stability depends on complex dependencies between the material parameters and the spatial and temporal grid resolution, the phase error solely depends on the spatial grid resolution and it disappears if the spatial grid resolution tends to ∞. The algorithm's accuracy also depends on the temporal resolution, i.e. on the size of the time-step because only in the limes where the time-step tends to 0, the numerical dispersion relation becomes equal to the physical dispersion relation of the simulated material.

First, the numerical dispersion relation which, in fact, represents the phase error of the algorithm is derived. Assume that each unknown in the system is represented as a plane wave of the form $e^{-i(\omega t - \mathbf{k}\mathbf{x})}$. Then, derivatives in the time-domain are replaced with multiplications of $-i\omega$ in the frequency domain, ∇ is replaced with $i\mathbf{k}$. With respect to the discretised space, ∂_t is replaced with $-i\Omega$ and ∇ with $i\mathbf{K}$ where (in a uniform grid with $\Delta = \Delta_{x,y,z}$ and axis along the unit vectors $\mathbf{e_{x,y,z}}$)

$$\Omega = \frac{2}{\Delta t} \sin\left(\frac{\omega \Delta t}{2}\right)$$

$$\mathbf{K} = \frac{2}{\Delta}\left[\sin\left(\frac{k_x \Delta}{2}\right)\mathbf{e_x} + \sin\left(\frac{\mathbf{k_y}\Delta}{2}\right)\mathbf{e_y} + \sin\left(\frac{\mathbf{k_z}\Delta}{2}\right)\mathbf{e_z}\right]$$

Clearly, as the step size and the cell size tend to 0, the above expressions reduce to their analytical counterparts. Using equations (5.1),(5.3) and (1.1b), applying the above expressions as described before and solving the resulting system, the numerical dispersion relation is found:

$$\mathbf{K} \cdot \mathbf{K}\mathbf{c^2} = \Omega^2 \epsilon_{\mathbf{num}} \qquad (5.11)$$

where the numerical permittivity is given by

$$\epsilon_{num} = \epsilon_\infty - \sum_d^D \frac{\omega_d^2}{\Omega^2 + i\delta_d\Omega}. \qquad (5.12)$$

Apparently, the loss term as well as the resonance frequency are misrepresented by the central difference expressions as the numerical spectral frequency Ω is only equal to the physical spectral frequency ω if $\Delta t = 0$, which is never the case. Thus, to obtain accurate solutions it is suggested that Δt should be chosen such that $\omega_{max}\Delta t$ is small (~ 0.1; ω_{max} is the maximum frequency in the initial waveform).

To derive a stability condition for $DADE^+$, (5.11) has to be solved for ω. Equation (5.11) is a complicated expression of frequency and wave number (and has to be solved numerically in the most general case of the algorithm). In order to solve it for ω analytically, it has to be assumed that the dielectric is lossless, i.e. $\delta = 0$, and the number of Drude-poles $D = 1$. This yields

$$\omega = \frac{2}{\Delta t} \arcsin \sqrt{\frac{S^2}{\epsilon_\infty} \left[\sin^2 \left(\frac{k_x \Delta}{2} \right) + \sin^2 \left(\frac{k_x \Delta}{2} \right) + \sin^2 \left(\frac{k_x \Delta}{2} \right) \right] + \frac{\omega_1^2 \Delta t^2}{4 \epsilon_\infty}} \quad (5.13)$$

$$\doteq \frac{2}{\Delta t} \arcsin \zeta \quad (5.14)$$

where S is the Courant-number. As soon as $\zeta > 1$, ω becomes imaginary and the algorithm enters the unstable regime. While the first term under the square root of the above equation can be made arbitrarily small by decreasing the grid resolution Δ, the second term indicates that the algorithm is only stable if

$$\omega_1 \Delta t \leq 2 \sqrt{\epsilon_\infty}. \quad (5.15)$$

This is only the largest value for which the algorithm is stable. Above this value, the algorithm is unstable independent of the grid resolution Δ. If the sin-terms do not vanish, then the above threshold value has to be reduced accordingly.

Next, the numerical wave number shall be derived and analysed. To this end, the one-dimensional case is considered and equation (5.11) is solved for k:

$$k = \frac{2}{\Delta} \arcsin \sqrt{\frac{1}{S^2} \left[\epsilon_\infty \sin^2 \left(\frac{\pi S}{N_\lambda} \right) - \frac{\omega_1^2 \Delta t^2}{4} \right]} \quad (5.16)$$

$$\doteq \frac{2}{\Delta} \arcsin \xi \quad (5.17)$$

where the sampling number $N_\lambda = \lambda / \Delta$ was used. Again, if $\xi > 1$ the numerical wave vector k becomes imaginary which leads to an aphysical exponential decay of the wave. As a result, a lower limit for the spatial grid sampling number N_λ is found to be

$$N_\lambda \geq \frac{\pi S}{\arcsin \sqrt{\left(\frac{S^2}{\epsilon_\infty} + \frac{\omega_1^2 \Delta t^2}{4 \epsilon_\infty} \right)}}. \quad (5.18)$$

It is interesting to note that in the case of the absence of any Drude-pole, i.e. $\omega_1 = 0$, the above expression reduces to the same expression that is obtained for the standard Yee-algorithm [3] (as one would expect). One has to be aware that S and N_λ depend on or determine Δ. A sufficiently large sampling of the traversing wave ensures that the wave will not aphysically decay and that the phase velocity is accurate. This fact is shown in figure 14 where the real (solid) and imaginary (dashed) parts of the phase velocity $v = \omega / k$ are shown as functions of the grid sampling number N_λ. For N_λ larger than the above threshold (5.18) (here around 2.7), the imaginary part vanishes and the

numerical phase velocity approaches the physical phase velocity. As it can be seen from figure 15, a higher grid sampling number increases the accuracy. Thus, the numerical phase velocity approaches the physical phase velocity to an arbitrary accuracy as long as the grid sampling number is large enough. All the results derived here were observed and verified using one-dimensional simulations in Matlab.
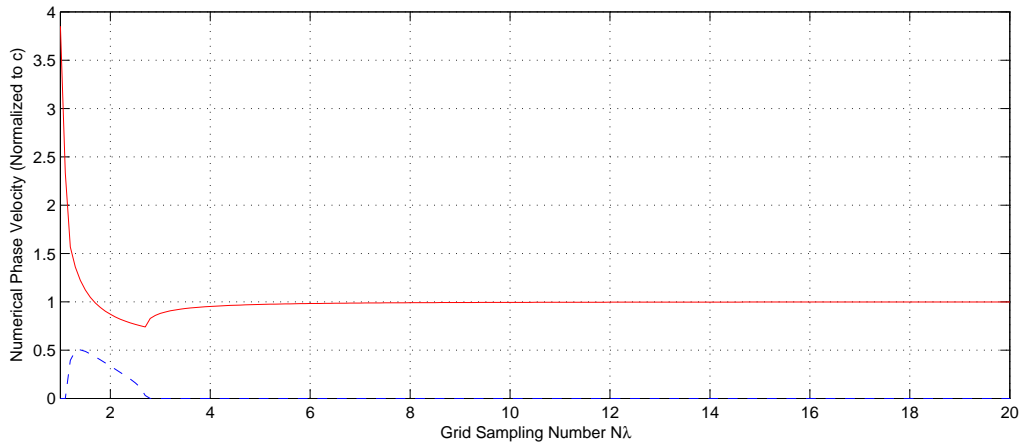
Figure 14: The real (solid line) and imaginary (dashed line) parts of the phase velocity $v = \omega/k$ of $DADE^+$ are shown as functions of the grid sampling number N_λ. For N_λ larger than ~ 2.7 (given by (5.18)), the imaginary part vanishes and the numerical phase velocity approaches the physical phase velocity.
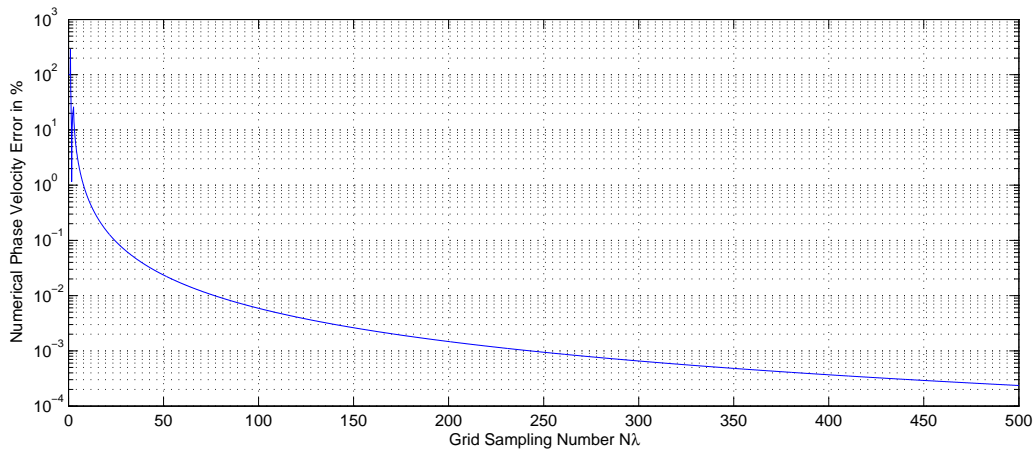
Figure 15: The plot shows the percental error of the phase velocity as a function of the grid sampling number N_λ of $DADE^+$. A higher N_λ ensures a higher accuracy.

5.1.4 Stability of DADE Algorithm

The stability and phase error of $DADE$ are very similar to those of $DADE^+$. The only difference is that due to central averaging a new factor arises which modifies the numerical permittivity. The numerical dispersion relation is given by

$$\mathbf{K} \cdot \mathbf{Kc^2} = \mathbf{\Omega^2}\epsilon_{\mathbf{num}} \tag{5.19}$$

where the numerical permittivity is given by

$$\epsilon_{num} = \epsilon_\infty - \sum_d^D \frac{\omega_d^2 \Lambda}{\Omega^2 + i\delta_d\Omega}. \tag{5.20}$$

where $\Delta\epsilon = \epsilon_s - \epsilon_\infty$ (ϵ_s is the static permittivity, i.e. permittivity at zero frequency). Λ is the factor mentioned above which has its origins in the central averaging and is given by

$$\Lambda = cos\left(\frac{\omega\Delta t}{2}\right).$$

Apparently, the loss term as well as the resonance frequency are misrepresented by the central difference expressions as the numerical spectral frequency Ω is only equal to the physical spectral frequency ω if $\Delta t = 0$, which is never the case. Thus, to obtain accurate solutions it is suggested that Δt should be chosen such that $\omega_{max}\Delta t$ is small (~ 0.1; ω_{max} is the maximum frequency in the initial waveform).

The dispersion relation can not be solved analytically for ω and has therefore to be solved numerically in the most general case of the algorithm. In order to derive an analytical solution for ω, it has to be assumed that the dielectric is lossless, i.e. $\delta = 0$, and the number of Lorentz-poles is $L = 1$. Furthermore it has to be assumed that $\omega\Delta t \approx 0$ such that the approximation $\Lambda = 1$ is valid. Under these conditions, the same conditions as for $DADE^+$ are valid and are hence not repeated.

5.1.5 Results

In the following, results of one-dimensional simulations performed with Matlab are shown. The interpretation of these results shall be explained here briefly and is shown in figure 16. The source is a 'hard source' which starts radiating at t=0 outside the medium in free space and stops radiating after a certain time. The generated light pulse moves away from the source when time passes. On the left hand side of the source, a first order mur simulates infinite free space, on the right hand side of the source begins the medium at 0 μm. A part of the beam is reflected, the rest is transmitted and phase- and group-velocity change. While the group-velocity is defined as traversed distance of the entire pulse over the passed time, i.e. by the inclination of the pulse-propagation, the group-velocity is defined as traversed distance of a phase-front over the passed time, i.e. by the inclination of the phase-fronts (thin lines) inside the pulse. In the explained example, one can readily see, that in free space, phase- and group-velocity are equal, as pulse and phase-fronts are parallel. Inside the medium, the phase-velocity is negative (as a DNM is simulated), while group-velocity is still positive, but slower than in free space.

Figure 16: The source is a 'hard source' which starts radiating at t=0 outside the medium in free space and stops radiating after a certain time. The generated light pulse moves away from the source when time passes. On the left hand side of the source, a first order mur simulates infinite free space, on the right hand side of the source begins the medium at 0 μm. A part of the beam is reflected, the rest is transmitted and phase- and group-velocity change. While the group-velocity is defined as traversed distance of the entire pulse over the passed time, i.e. by the inclination of the pulse-propagation, the group-velocity is defined as traversed distance of a phase-front over the passed time, i.e. by the inclination of the phase-fronts (thin lines) inside the pulse. One can readily see, that in free space, phase- and group-velocity are equal, as pulse and phase-fronts are parallel. Inside the medium, the phase-velocity is negative (as a DNM is simulated), while group-velocity is still positive, but slower than in free space.
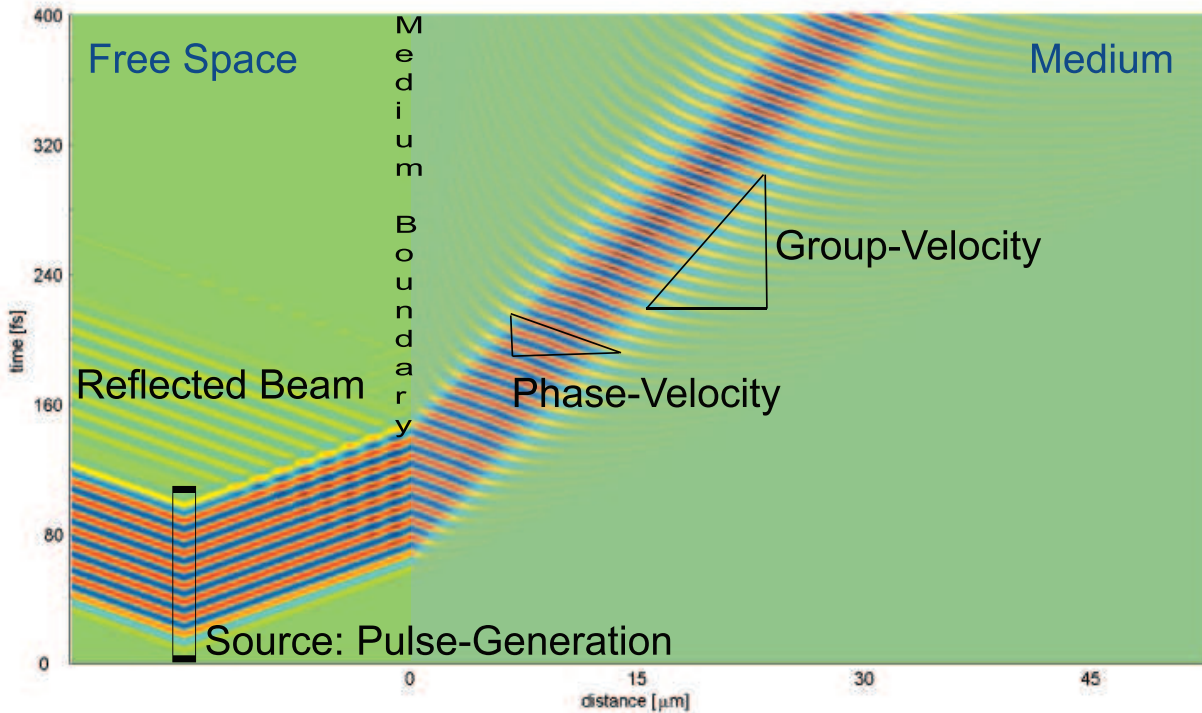
$DADE$ and $DADE^+$ were implemented in Matlab in a one-dimensional model. Figure 17 shows how a pulse generated in free space enters a medium with a single Drude pole. Absorption was neglected by setting the damping of the Drude-oscillator to $\delta = 0$. It can be readily seen that the longer the pulse propagates through the medium, the stronger it gets broadened. Furthermore it can be seen that the phase velocity remains the same because the slope of the phase-fronts (small lines inside the pulse) remains the same. This is because the dispersion parameters were chosen in a manner such that $\epsilon(\omega_0) = 1$ inside the medium where ω_0 is the carrier frequency. The group velocity, however, which is the propagation velocity of the pulse is reduced compared with the free space propagation speed. This is seen because the slope of the pulse propagation is increased.
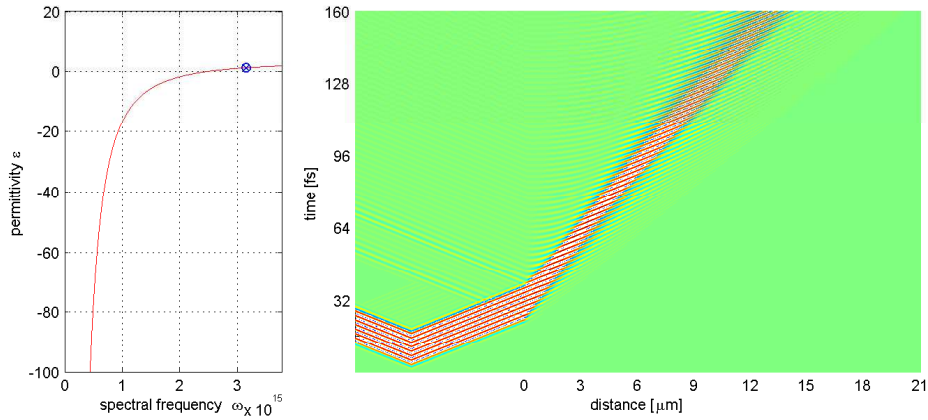
Figure 17: Left: Course of the permittivity in a Drude-medium with indicated location of the carrier-frequency of the pulse. Right: A light-pulse is generated in free space and enters a Drude-medium at 0. Pulse-broadening and change of group-velocity can be readily seen.
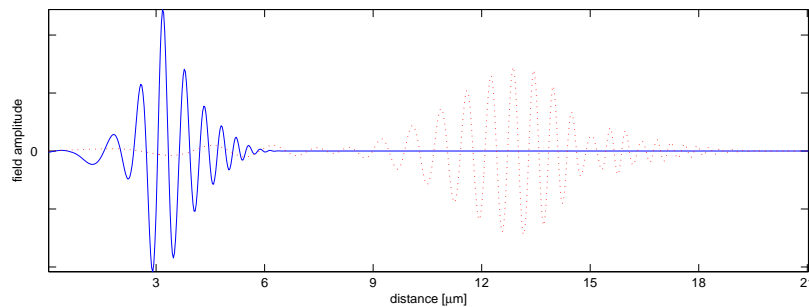

Figure 18: The light-pulse of the previous figure 17 inside the Drude-medium at 64 fs (solid) and 160 fs (dotted) after pulse generation. Pulse broadening can be readily seen.

5.2 Lorentz Medium with ADE-FDTD

Two different ADE-FDTD algorithms for Lorentz dispersive media will be introduced next. The difference lies in the number of stored variables and in accuracy while computational speed is equal.

5.2.1 Formalism with Polarisation

The derivation of the Lorentz auxiliary differential equation is analogous to the above derivation of the Drude differential equation for $DADE^+$ algorithm. Consider a multiterm Lorentz dispersive medium having a total of L poles in its susceptibility response. Again, Ampere's law (5.1) can be used with $\mathbf{P_l}$ the polarization current associated with the lth Lorentz pole. Recalling equation (2.10) of the Lorentz-oscillator one can write in the frequency domain

$$\mathbf{P_l}(\omega) = \epsilon_0 \chi_L^1 E(\omega)$$
$$= \frac{\epsilon_0 \Delta\epsilon_l \omega_l^2}{\omega_l^2 - \omega^2 - 2i\omega\delta_l} E(\omega). \tag{5.21}$$

Multiplication of both sides of the above equation with $(\omega_l^2 - \omega^2 - 2i\omega\delta_l)$ gives

$$\omega_l^2 \mathbf{P_l}(\omega) - \mathbf{2i}\omega\delta_l \mathbf{P_l}(\omega) - \omega^2 \mathbf{P_l}(\omega) = \epsilon_0 \boldsymbol{\Delta}\epsilon_l \omega_l^2 \mathbf{E}(\omega).$$

Now, a Fourier-transformation yields the desired ADE:

$$\omega_l^2 \mathbf{P_l}(\mathbf{t}) + \ddot{\mathbf{P}}_\mathbf{l}(\mathbf{t}) + \mathbf{2}\delta_l \dot{\mathbf{P}}_\mathbf{l}(\mathbf{t}) = \epsilon_0 \boldsymbol{\Delta}\epsilon_l \omega_l^2 \mathbf{E}(\mathbf{t}) \tag{5.22}$$

Applying finite-difference expressions for the partial derivations to (5.22) and some algebraic manipulation yields the desired update scheme for $\mathbf{P_p}$:

$$\mathbf{P_l^{n+1}} = \alpha_l \mathbf{P_l^n} + \beta_l \mathbf{P_l^{n-1}} + \gamma_l \mathbf{E^n} \tag{5.23}$$

with the update coefficients

$$\alpha_l = \frac{2 - \omega_l^2 \Delta t^2}{1 + \delta_l \Delta t}$$
$$\beta_l = \frac{1 - \delta_l \Delta t}{1 + \delta_l \Delta t}$$
$$\gamma_l = \frac{\epsilon_0 \Delta\epsilon_l \omega_l^2 (\Delta t)^2}{1 + \delta_l \Delta t}$$

The update equation for the electric field can then be derived by evaluating Ampere's law (5.1) at time step $n + \frac{1}{2}$, which was already derived in the previous section and is given by equation (5.5).

Thus, the algorithm starts with the electric field update via (5.5), then the polarization currents are updated via (5.23). In the concluding step, the magnetic field is updated via equation (4.1a), which completes the algorithm. In the rest of this document, this

algorithm will be referred to as $LADE^+$ algorithm. The + indicates that this algorithm has better performance as it requires to store one variable less than the $LADE$ algorithm which will be derived next. It is not clear whether $LADE^+$ has also increased accuracy like $DADE^+$ has or not. But higher accuracy can be expected because, as it will be shown in the sections 5.2.3 and 5.2.4, the numerical permittivity of $LADE^+$ is closer to the exact permittivity than $LADE$ because no central averaging has to be done. While numerical experiments did not exhibit any drastic differences, further experimental analysis of $LADE^+$'s exactness is suggested.

5.2.2 Formalism with Polarisation Current

The derivation of the Lorentz auxiliary differential equation is analogous to the above derivation of the Drude differential equation for the $DADE$ algorithm. Consider a multiterm Lorentz dispersive medium having a total of L poles in its susceptibility response. Again, Ampere's law (5.6) can be used with $\mathbf{J_l}$ the polarization current associated with the lth Lorentz pole. Recalling equation (2.10) of the Lorentz-oscillator one can write in the frequency domain

$$\mathbf{J_l}(\omega) = -i\omega\epsilon_0\chi_L^1 E(\omega)$$
$$= -i\omega\frac{\epsilon_0\Delta\epsilon_l\omega_l^2}{\omega_l^2 - \omega^2 - 2i\omega\delta_l}E(\omega). \tag{5.24}$$

Multiplication of both sides of the above equation with $(\omega_l^2 - \omega^2 - i\omega\delta_l)$ gives

$$\omega_l^2\mathbf{J_l}(\omega) - 2i\omega\delta_l\mathbf{J_l}(\omega) - \omega^2\mathbf{J_l}(\omega) = -i\epsilon_0\Delta\epsilon_l\omega_l^2\omega\mathbf{E}(\omega).$$

Now, a Fourier-transformation brings the above equation back to the time-domain and yields the desired ADE:

$$\omega_l^2\mathbf{J_l(t)} + \ddot{\mathbf{J}}_\mathbf{l}(\mathbf{t}) + 2\delta_l\dot{\mathbf{J}}_\mathbf{l}(\mathbf{t}) = +\epsilon_0\Delta\epsilon_l\omega_l^2\dot{\mathbf{E}}(\mathbf{t}) \tag{5.25}$$

Applying finite-difference expressions for the partial derivations to (5.25) and some algebraic manipulation yields the desired update scheme for $\mathbf{J_l}$:

$$\mathbf{J_l^{n+1}} = \alpha_l\mathbf{J_l^n} + \beta_l\mathbf{J_l^{n-1}} + \gamma_l\left(\frac{\mathbf{E^{n+1}} - \mathbf{E^{n-1}}}{\mathbf{2\Delta t}}\right) \tag{5.26}$$

with the update coefficients

$$\alpha_l = \frac{2 - \omega_l^2(\Delta t)^2}{1 + \delta_l\Delta t}$$
$$\beta_l = \frac{\delta_l\Delta t - 1}{1 + \delta_l\Delta t}$$
$$\gamma_l = \frac{\epsilon_0\Delta\epsilon_l\omega_l^2(\Delta t)^2}{1 + \delta_l\Delta t}$$

The update equation for the electric field can then be derived by evaluating Ampere's law (5.6) at time step $n + \frac{1}{2}$:

$$\mathbf{E^{n+1}} = \mathbf{C_1 E^{n-1}} + \mathbf{C_2 E^n} + \mathbf{C_3} \left(\nabla \wedge \mathbf{H^{n+\frac{1}{2}}} - \frac{1}{2} \sum_{l=1}^{L} \left[(1 + \alpha_l) \mathbf{J_l^n} + \xi_l \mathbf{J_l^{n-1}} \right] \right) \qquad (5.27)$$

with the update coefficients

$$C_1 = \frac{\frac{1}{2} \sum_{l=1}^{L} \gamma_l}{2\epsilon_0 \epsilon_\infty + \frac{1}{2} \sum_{l=1}^{L} \gamma_l + \sigma \Delta t}$$

$$C_2 = \frac{2\epsilon_0 \epsilon_\infty - \sigma \Delta t}{2\epsilon_0 \epsilon_\infty + \frac{1}{2} \sum_{l=1}^{L} \gamma_l + \sigma \Delta t}$$

$$C_3 = \frac{2\Delta t}{2\epsilon_0 \epsilon_\infty + \frac{1}{2} \sum_{l=1}^{L} \gamma_l + \sigma \Delta t}$$

Thus, the algorithm starts with the electric field update via (5.27), then the polarization currents are updated via (5.26). In the concluding step, the magnetic field is updated via equation (4.1a), which completes the algorithm. This algorithm will be referred to as *LADE* algorithm in the rest of this document.

5.2.3 Stability of $LADE^+$ Algorithm

In this section, the stability and phase error of $LADE^+$ will be derived. The used methodology is presented in [3] and [31]. The analysis is completely analogous to the one performed in section 5.1.3. As a result, a stability condition is found which determines how to chose the spatial sampling Δ and the temporal sampling Δt. Using the same notation as in section 5.1.3 and applying the previously described analysis to equations (5.1),(5.22) and (1.1b) yields the numerical dispersion relation

$$\mathbf{K} \cdot \mathbf{K} c^2 = \Omega^2 \epsilon_{\mathbf{num}} \qquad (5.28)$$

where the numerical permittivity is given by

$$\epsilon_{num} = \epsilon_\infty + \sum_{l}^{L} \frac{\Delta \epsilon \omega_l^2}{\omega_l^2 - \Omega^2 - 2i\delta_l \Omega} \qquad (5.29)$$

where $\Delta \epsilon = \epsilon_s - \epsilon_\infty$ (ϵ_s is the static permittivity, i.e. permittivity at zero frequency). Apparently, the loss term as well as the resonance frequency are misrepresented by the central difference expressions as the numerical spectral frequency Ω is only equal to the physical spectral frequency ω if $\Delta t = 0$, which is never the case. Thus, to obtain accurate solutions it is suggested that Δt should be chosen such that $\omega_{max} \Delta t$ is small (~ 0.1; ω_{max} is the maximum frequency in the initial waveform).

To derive a stability condition for $LADE^+$, (5.28) has to be solved for ω. Equation (5.28) is a complicated expression of frequency and wave number (and has to be solved numerically in the most general case of the algorithm). In order to solve it for ω analytically, it has

to be assumed that the dielectric is lossless, i.e. $\delta = 0$, and the number of Lorentz-poles $L = 1$. First, equation (5.28) is solved for Ω^2 giving

$$\Omega^2 = \frac{\mathbf{K} \cdot \mathbf{Kc^2} + \epsilon_s \omega_1^2 + \sqrt{(\mathbf{K} \cdot \mathbf{Kc^2} + \epsilon_s \omega_1^2)^2 + \epsilon_\infty \mathbf{K} \cdot \mathbf{Kc^2} \omega_1^2}}{2\epsilon_\infty}. \qquad (5.30)$$

Now, solving the above equation for ω yields

$$\omega = \frac{2}{\Delta t} \arcsin \sqrt{\frac{\Delta t \Omega}{2}} \qquad (5.31)$$

$$\doteq \frac{2}{\Delta t} \arcsin \zeta \qquad (5.32)$$

where (in one dimension)

$$\zeta = \sqrt{\frac{1}{2\epsilon_\infty} \left(\chi_1 + \sqrt{\chi_1^2 + \chi_2^2} \right)} \qquad (5.33)$$

with

$$\chi_1 = S^2 \sin^2 \left(\frac{k\Delta}{2} \right) + \frac{\epsilon_s}{4} \Delta t^2 \omega_1^2$$

$$\chi_2 = 2S \sin \left(\frac{k\Delta}{2} \right) \Delta t \omega_1.$$

As soon as $\zeta > 1$, ω becomes imaginary and the algorithm enters the unstable regime. While the terms of the above equation proportional to sin can be made arbitrarily small by decreasing the grid resolution Δ, the remaining terms indicate that the algorithm is only stable if

$$\Delta t \omega_1 \leq 2\sqrt{\frac{\epsilon_\infty}{\epsilon_s}} \qquad (5.34)$$

This is only the largest value for which the algorithm is stable. Above this value, the algorithm is unstable independent of the grid resolution Δ. If the sin-terms do not vanish, then the above threshold value has to be reduced accordingly.

Next, the numerical wave number shall be derived and analysed. To this end, the one-dimensional case is considered and equation (5.28) is solved for k:

$$k = \frac{2}{\Delta} \arcsin \left(\frac{1}{S} \sin \left(\frac{\pi S}{N_\lambda} \right) \sqrt{\epsilon_\infty + \frac{\Delta \epsilon \omega_1^2 \Delta t^2}{\omega_1^2 \Delta t^2 - 4\sin^2 \left(\frac{\pi S}{N_\lambda} \right)}} \right) \qquad (5.35)$$

$$\doteq \frac{2}{\Delta} \arcsin \xi \qquad (5.36)$$

where the sampling number $N_\lambda = \lambda/\Delta$ was used. Again, if $\xi > 1$ the numerical wave vector k becomes imaginary which leads to an aphysical exponential decay of the wave. The above equation cannot be solved analytically for N_λ. Nevertheless, a lower limit for the sampling number N_λ can be derived for the physically relevant case $\epsilon_s \geq 1$. This will be done next. First, some abbreviations are introduced:

$$y = \sin^2\left(\frac{\pi S}{N_\lambda}\right)$$
$$z = \omega_1^2 \Delta t^2.$$

The condition for stability (no aphysical exponential decay of the wave) $\xi \leq 1$ can then be rewritten as

$$y(\epsilon_s z - 4y) \leq S^2(z - 4y) \tag{5.37}$$

which cannot be solved for y. The problems of the above equation can be bypassed by introducing an arbitrary constant b and having in mind that $\epsilon_s \geq 1$:

$$z = \frac{b}{\epsilon_s} \leq b \tag{5.38}$$

Where the first equality defines the constant b. This is now applied to inequality (5.37).

$$\begin{aligned}
y(\epsilon_s z - 4y) &= y(b - 4y) \\
&\leq S^2\left(\frac{b}{\epsilon_s} - 4y\right) \\
&\leq S^2(b - 4y).
\end{aligned} \tag{5.39}$$

Thus, the condition for the sampling number N_λ to prevent a wave from aphysically decaying is

$$N_\lambda \geq \frac{\pi S}{\arcsin S}. \tag{5.40}$$

This is the same condition that is found for the standard Yee-algorithm [3]. This equality has probably to be attributed to the fact that a second inequality , i.e. $b \leq b\epsilon_s$, had to be used in its derivation. The course of the numerical phase velocity as a function of the grid sampling number is very similar to the one of $DADE^+$ presented in section 5.1.3 and are hence analogue to figure 14. Also the percental phase velocity error is very similar to the one of $DADE^+$ and its course as a function of the grid sampling number are hence analogue to figure 15. One has to be aware here that S and N_λ depend on or determine Δ. A sufficiently large sampling of the traversing wave ensures that the wave will not aphysically decay. All the results derived here were observed and thus verified in a one-dimensional simulation in Matlab.

5.2.4 Stability of LADE Algorithm

The stability and phase error of $LADE$ are very similar to those of $LADE^+$. The only difference is that due to central averaging a new factor arises which modifies the numerical permittivity. The numerical dispersion relation is still given by

$$\mathbf{K} \cdot \mathbf{K}\mathbf{c^2} = \mathbf{\Omega^2}\epsilon_{\mathbf{num}} \tag{5.41}$$

where the numerical permittivity is given by

$$\epsilon_{num} = \epsilon_\infty + \sum_l^L \frac{\Delta\epsilon\omega_l^2\Lambda}{\omega_l^2 - \Omega^2 - 2i\delta_l\Omega} \tag{5.42}$$

where $\Delta\epsilon = \epsilon_s - \epsilon_\infty$ (ϵ_s is the static permittivity, i.e. permittivity at zero frequency). Λ is the factor mentioned above which origins in the central averaging and is given by

$$\Lambda = cos\left(\frac{\omega\Delta t}{2}\right).$$

Apparently, the loss term as well as the resonance frequency are misrepresented by the central difference expressions as the numerical spectral frequency Ω is only equal to the physical spectral frequency ω if $\Delta t = 0$, which is never the case. Thus, to obtain accurate solutions it is suggested that Δt should be chosen such that $\omega_{max}\Delta t$ is small (~ 0.1; ω_{max} is the maximum frequency in the initial waveform).

The dispersion relation can not be solved analytically for ω and has therefore to be solved numerically in the most general case of the algorithm. In order to derive an analytical solution for ω, it has to be assumed that the dielectric is lossless, i.e. $\delta = 0$, and the number of Lorentz-poles $L = 1$. Furthermore it has to be assumed, that the term $\omega\Delta t \approx 0$ such that the approximation $\Lambda = 1$ is valid. Under these conditions, the same conditions as for $LADE^+$ are valid and are hence not repeated.

5.2.5 Results

$LADE$ and $LADE^+$ were implemented in Matlab in a one-dimensional model. Figure 19 shows how a pulse generated in free space enters a medium with a single Drude pole in its permittivity and the course of the latter. Absorption was neglected by setting the damping of the Lorentz-oscillator $\delta = 0$. It can be seen readily that the longer the pulse propagates through the medium, the stronger it gets broadened 20. Furthermore it can be seen that the phase velocity changes slightly because the slope of the phase-fronts (small lines inside the pulse) is increased. This is because the dispersion parameters were chosen in a manner such that $\epsilon(\omega_0) = 1.1$ inside the medium where ω_0 is the carrier frequency. The group velocity which is the propagation velocity of the pulse is reduced compared with the free space propagation speed. This is seen because the slope of the pulse propagation is increased.
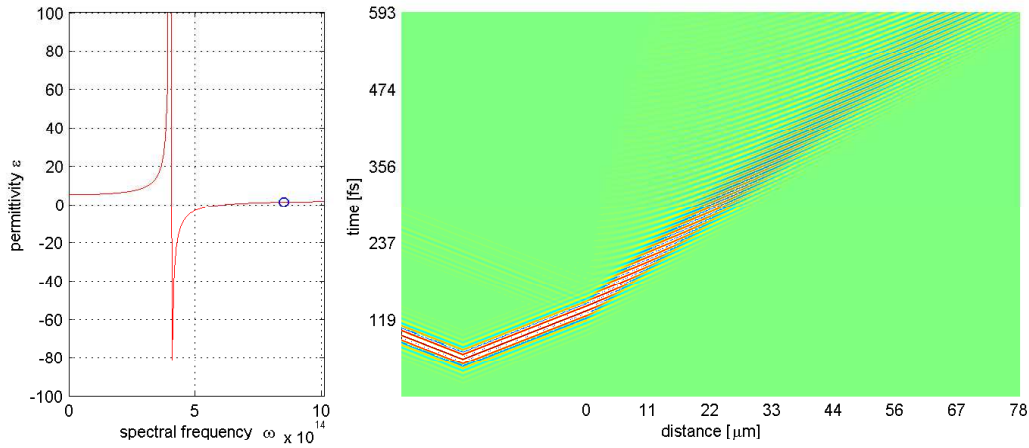
Figure 19: Left: Course of the permittivity in a Lorentz-medium with indicated location of the carrier-frequency of the pulse. Right: A light-pulse is generated in free space and enters a Lorentz-medium at 0. Pulse-broadening and change of group-velocity can be readily seen.
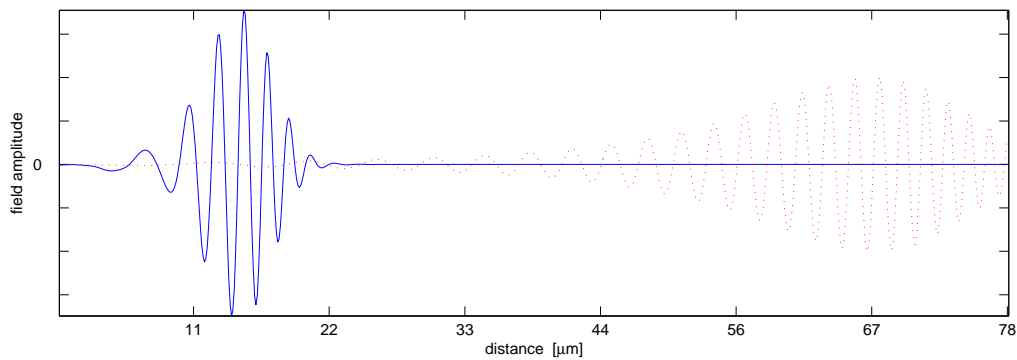

Figure 20: The light-pulse of the previous figure 19 inside the Lorentz-medium at 237 fs (solid) and 593 fs (dotted) after pulse generation. Pulse broadening can be readily seen.

5.3 Debye Medium with ADE-FDTD

For the sake of completeness the ADE-FTDT update schemes of a Debye medium are reproduced here. The derivation is not repeated, as it is analogous to the derivation of the previous algorithms where the derivation was performed already at length.

5.3.1 Formalism with Polarisation

Ampere's Law (5.1) is used again. The update of the polarization $\mathbf{P_p}$ of the pth Debye dipole with relaxation time τ_p is given by the finite-difference expression of equation (2.15) centered at time step n:

$$\mathbf{P_p^{n+1}} = \alpha_\mathbf{p}\mathbf{P_p^n} + \mathbf{P_p^{n-1}} - \beta_\mathbf{p}\mathbf{E^n} \tag{5.43}$$

with update coefficients

$$\alpha_p = \frac{2\Delta t}{\tau_p}$$
$$\beta_p = \frac{2\epsilon_0 \Delta t \Delta\epsilon}{\tau_p}.$$

The electric field update equation is then given by (5.5). This algorithm will be referred to as $ADeb^+$.

5.3.2 Formalism with Polarisation Current

Ampere's Law (5.6) is used again. The update of the polarization current $\mathbf{J_p}$ of the pth Debye dipole with relaxation time τ_p is given by

$$\mathbf{J_p^{n+1}} = \alpha_\mathbf{p}\mathbf{J_p^n} + \beta_\mathbf{p}(\mathbf{E^{n+1}} - \mathbf{E^n}) \tag{5.44}$$

with update coefficients

$$\alpha_p = \frac{1 - \frac{\Delta t}{2\tau_p}}{1 + \frac{\Delta t}{2\tau_p}}$$
$$\beta_p = \frac{\Delta\epsilon\delta t/\tau_p}{1 + \frac{\Delta t}{2\tau_p}}.$$

The electric field update equation is then given by

$$\mathbf{E^{n+1}} = \mathbf{C_1}\mathbf{E^n} + \mathbf{C_2}\left[\nabla \wedge \mathbf{H^{n+\frac{1}{2}}} - \frac{1}{2}\sum_{\mathbf{p=1}}^{\mathbf{N}}(1 + \alpha_\mathbf{p})\mathbf{J_p^n}\right] \tag{5.45}$$

with update coefficients

$$C_1 = \frac{2\epsilon_0\epsilon_\infty + \sum_{p=1}^{N}\beta_p - \sigma\Delta t}{2\epsilon_0\epsilon_\infty + \sum_{p=1}^{N}\beta_p + \sigma\Delta t}$$
$$C_2 = \frac{2\Delta t}{2\epsilon_0\epsilon_\infty + \sum_{p=1}^{N}\beta_p + \sigma\Delta t}.$$

This algorithm will be referred to as $ADeb$.

5.4 Comparison of Algorithms

The six algorithms presented so far are compared briefly and their most interesting aspects are pointed out.

Drude ADE-FDTD $DADE^+$ needs to store one variable per grid point more than $DADE$. [32] reports higher accuracy for the $DADE^+$ algorithm at the same computational speed. $DADE^+$ shows excellent stability when the conditions derived in section 5.1.3 are satisfied. $DADE$ algorithm is stable with similar conditions that are a little bit less restrictive (this was found empirically).

Lorentz ADE-FDTD $LADE^+$ needs to store one variable per grid point more than $LADE$. Also [32] reports higher accuracy for the $LADE^+$ algorithm at the same computational speed. $LADE^+$ shows excellent stability when the conditions derived in section 5.2.3 are satisfied. $LADE$ algorithm is stable with similar conditions that are a little bit less restrictive (this was found empirically).

Debye ADE-FDTD $ADeb^+$ needs to store one variable per grid point more than $ADeb$. It was found empirically that $ADeb^+$ is only stable as long as $\omega > 4 \cdot 2\pi/\tau_p$ and for approximately 500 time steps. After these 500 time steps instability oscillations at the material boundary start to increase exponentially. $ADeb$ is stable in all regimes as long as $S \leq 1$.

It can be said generally that the algorithms involving the polarisation-current instead of the polarisation are more stable in the sense that their stability conditions seem to be less restrictive. However, stability can always be ensured by decreasing the time step.

5.5 Non-linear Effects with ADE-FDTD

In order to implement a non-linear material model with ADE-FDTD, the approach of [2] will be followed who proposed a full-vector Maxwell's equations solution incorporating multiple-pole linear Lorentz, non-linear Kerr and non-linear Raman polarization. This algorithm can be easily applied to other material models, but it requires a Newton-iteration to solve a non-linear equation and hence computation time is drastically increased. This algorithm will be called $GVADE$ (General Vector ADE) hereafter, as done by [2].

As there are now several different contributions of polarisation currents to Ampere's law, it is rewritten as

$$\nabla \wedge \mathbf{H} = \epsilon_0 \epsilon_\infty \frac{\partial \mathbf{E}}{\partial t} + \sum_{p=1}^{N} \mathbf{J_{Lorentz_p}} + \mathbf{J_{Kerr}} + \mathbf{J_{Raman}} + \sigma \mathbf{E}. \tag{5.46}$$

Centering of the above equation at time-step $n + \frac{1}{2}$ yields

$$\nabla \wedge \mathbf{H^{n+\frac{1}{2}}} = \epsilon_0 \epsilon_\infty \frac{\mathbf{E^{n+1}} - \mathbf{E^n}}{\Delta t} + \sum_{p=1}^{N} \mathbf{J_{Lorentz_p}^{n+\frac{1}{2}}} + \mathbf{J_{Kerr}^{n+\frac{1}{2}}} + \mathbf{J_{Raman}^{n+\frac{1}{2}}} + \sigma \frac{\mathbf{E^{n+1}} + \mathbf{E^n}}{2}, \tag{5.47}$$

which is in fact the update equation for the electric field $\mathbf{E}$.

Next, the update equations for the different polarization currents have to be derived. As it can be seen in equation (5.47), all polarization currents have to be centered at time-step $n + \frac{1}{2}$.

5.5.1 Lorentz-Dispersion

The contribution to the polarisation currents by the pth Lorentz-pole $\mathbf{J_{Lorentz_p}}$ was derived in section 5.2. [2] uses a simpler version (without electric currents, i.e. $\sigma = 0$) of the update equation (5.26) for $\mathbf{J_{Lorentz_p}}$ of the $LADE$-algorithm.

5.5.2 Kerr-Effect

The contribution to the polarisation currents by the Kerr-effect $\mathbf{J_{Kerr}}$ was derived in section 2.3.2. Thus, the equation for $\mathbf{J_{Kerr}}$ is obtained directly by the finite-difference expression of equation (2.19) centered at time-step $n + \frac{1}{2}$:

$$\mathbf{J_{Kerr}^{n+\frac{1}{2}}} = \alpha \epsilon_0 \chi_0^3 \left(|\mathbf{E^{n+1}}|^2 \mathbf{E^{n+1}} - |\mathbf{E^n}|^2 \mathbf{E^n} \right) \tag{5.48}$$

5.5.3 Raman-Scattering

The contribution to the polarisation currents by Raman-scattering $\mathbf{J_{Raman}}$ was derived in section 2.3.2. Equation (2.20) is solved by introducing a scalar auxiliary variable for the convolution:

$$R(t) \doteq \chi_{Raman}^3(t) * |\mathbf{E(t)}|^2. \tag{5.49}$$

Taking the Fourier transform of the above equation brings it to the frequency domain, where $\chi^3_{Raman}(\omega)$ is described by

$$\chi^3_{Raman}(\omega) = \frac{(1-\alpha)\chi^3_0\omega^2_R}{\omega^2_R + 2i\omega\delta_R - \omega^2}$$

with

$$\omega_R = \sqrt{\frac{\tau^2_1 + \tau^2_2}{\tau^2_1\tau^2_2}},$$

$$\delta_R = \frac{1}{\tau_2}.$$

Multiplying both sides with $(\omega^2_R + 2i\omega\delta_R - \omega^2)$ and transforming back to the time domain yields

$$\omega^2_R R(t) + 2\delta_R \dot{R}(t) + \ddot{R}(t) = (1-\alpha)\chi^3_0\omega^2_R|\mathbf{E(t)}|^{\mathbf{2}}. \tag{5.50}$$

Applying finite-difference expressions centered at time step n to this equation yields the update equation for $R(t)$:

$$R^{n+1} = \left(\frac{2 - \omega_R\Delta t^2}{\delta_R\Delta t + 1}\right) R^n + \left(\frac{\delta_R\Delta t - 1}{\delta_R\Delta t + 1}\right) R^{n-1} + \left(\frac{(1-\alpha)\chi^3_0\omega^2_R\Delta t^2}{\delta_R\Delta t + 1}\right) |\mathbf{E^n}|^{\mathbf{2}}. \tag{5.51}$$

Herewith the finite-difference expression of equation (2.20) centered at time step $n + \frac{1}{2}$ becomes

$$\mathbf{J^{n+\frac{1}{2}}_{Raman}} = \epsilon_0 \frac{\mathbf{E^{n+1}R^{n+1} - E^nR^n}}{\mathbf{\Delta t}}. \tag{5.52}$$

Now that all variables of the finite-difference expression of Ampere's law (5.47) are known, it can be solved for $\mathbf{E^{n+1}}$. One notices that equation (5.47) is non-linear in $\mathbf{E^{n+1}}$ as could be expected because of the non-linear effects that are modelled by this algorithm. In order to solve this non-linear equation, [2] uses a simple Newton-iteration which solves for $\mathbf{E^{n+1}}$. This approach gives accurate results but is quite expensive in terms of computational operations (computation of an inverse 3×3-matrix plus iteration) that have to be performed at each Yee-mesh-point. It is hence very slow compared to the standard Yee algorithm or algorithms that only include linear dispersion.

In order to have one algorithm covering as many different material effects as possible, the Newton-iteration proposed by [2] is bad from a view of computational speed because Newton-iteration is only necessary for the non-linear term which origins from the Kerr-effect. All other effects such as Lorentz- and Drude-dispersion or the Raman-scattering are linear in $\mathbf{E}$ (as can be seen from their update equations) and do not require the Newton-iteration. For the latter, the Newton-iteration produces accurate results but at a very high computational cost.

In Part III (section 6 ff) a new algorithm is proposed that allows to control which material properties are included while at the same time computational speed is increased and the accuracy maintained.

5.5.4 Stability of GVADE

Both Kerr-effect and Raman-scattering result in a intensity dependent refractive index. Therefore, it can be expected that the stability conditions for $GVADE$ also depend on the intensity of the field.

Stability of Kerr-Effect   For the Kerr-effect one finds the simple numerical dispersion relation

$$\epsilon_{num} = \epsilon_\infty + \alpha\chi^3 I. \tag{5.53}$$

Which is similar to the standard Yee-algorithm dispersion with an intensity dependent permittivity. Solving the numerical dispersion relation

$$\mathbf{K} \cdot \mathbf{Kc^2} = \mathbf{\Omega^2}\epsilon_{\mathbf{num}} \tag{5.54}$$

for ω in one dimension yields

$$\omega = \frac{2}{\Delta t} \arcsin \sqrt{\frac{S^2 \sin^2\left(\frac{k\Delta}{2}\right)}{\epsilon_\infty + \alpha\chi^3 I}} \tag{5.55}$$

$$= \frac{2}{\Delta t} \arcsin \zeta. \tag{5.56}$$

As a consequence, ω becomes imaginary if $\zeta > 1$. Using the maximal value ζ can reach ($\sin = 1$), the following stability condition is found

$$S \leq \sqrt{\epsilon_\infty + \alpha\chi^3 I} \tag{5.57}$$

As expected, this condition depends on the field intensity and it seems that stability is increased with increasing intensity as the Courant-number S is not limited by ϵ_∞, but by the intensity. But this condition only ensures stability of the FDTD-algorithm itself. Solving the update equation for the Kerr-effect requires to solve a non-linear equation. This has to be done either by the Newton-method used in [2] or by applying a fixed-point iteration as described in section 6. If these iterations converge depends on the intensity of the applied field as shown in section 7.1. As a consequence, the above condition does not ensure stability of the entire algorithm, but it needs to be satisfied.

To determine the minimal grid sampling number N_λ, the numerical phase vector k which is given by

$$k = \frac{2}{\Delta} \arcsin \left[\frac{\sqrt{\epsilon_\infty + \alpha\chi^3 I}}{S} \sin \left(\frac{\pi S}{N_\lambda}\right) \right] \tag{5.58}$$

$$= \frac{2}{\Delta} \arcsin \xi \tag{5.59}$$

has to be analysed. If $\xi > 1$, then k becomes imaginary which results in an aphysical exponential decay of the wave. This is the case if the grid sampling number N_λ is too

small, i.e. it is required that

$$N_\lambda \geq \frac{\pi S}{\arcsin\left(\frac{S}{\epsilon_\infty + \alpha \chi^3 I}\right)}.$$

(5.60)

As the intensity is increased, the sampling number N_λ has to be increased as well. The course of the numerical phase velocity is very similar to the one presented in section 5.1.3 and can thus be seen in figure 14. The phase velocity error is analogous to the one found for the standard Yee-algorithm and can be seen in figure 15. All the results derived here were observed and hence verified in a one-dimensional simulation in Matlab.

Stability of Raman-Scattering   It can be readily seen that the Raman-scattering is proportional to a Lorentz-pole with pole-frequency ω_R whose stability was already discussed in section 5.2.3. The only difference is, that the term $\Delta\epsilon$ has to be replaced by $(1-\alpha)\chi^3|\mathbf{E}|^2$ and hence $\epsilon_s = (1-\alpha)\chi^3|\mathbf{E}|^2 + \epsilon_\infty$. The rest of the analysis is completely analogous to the one performed in section 5.2.3. Because the same conditions remain valid the results shall not be repeated.

Part III
Novel Approach for an Algorithm for Arbitrary Dispersive Materials

In this part, a novel and efficient algorithm is proposed which covers the linear Lorentz- and Drude-dispersion as well as the non-linear Kerr-effect and Raman-scattering. While it maintains the accuracy of the previously introduced algorithms $DADE^+$ and $LADE^+$ it is faster than the $GVADE$ algorithm proposed by [2] especially when the Kerr-effect is included.

6 Arbitrary Dispersive Material Algorithm

The algorithm for a general dispersive material is derived first. The algorithm will be referred to as $ADM+$ in the rest of this document. Most of the required update equations were already derived in Part II and will not be reproduced here.

6.1 Arbitrary Dispersive Permittivity

Consider Ampere's law

$$
\begin{aligned}
\nabla \wedge \mathbf{H} &= \frac{\partial \mathbf{D}}{\partial t} + \mathbf{j} \\
&= \epsilon_0 \epsilon_\infty \frac{\partial \mathbf{E}}{\partial t} + \frac{\partial \mathbf{P_{tot}}}{\partial t} + \sigma \mathbf{E}
\end{aligned} \tag{6.1}
$$

assuming that Ohm's law $\mathbf{j} = \sigma \mathbf{E}$ is valid. For a medium with L Lorentz-poles, D Drude-poles exhibiting Raman-scattering and Kerr-effect, the total polarisation $\mathbf{P_{tot}}$ can be written as

$$
\mathbf{P_{tot}} = \sum_{\mathbf{l=1}}^{\mathbf{L}} \mathbf{P_l} + \sum_{\mathbf{d=1}}^{\mathbf{D}} \mathbf{P_d} + \mathbf{P_{Kerr}} + \mathbf{P_{Raman}} \tag{6.2}
$$

The finite-difference expression of Ampere's law (6.1) centered at time step $n + \frac{1}{2}$ is

$$
\nabla \wedge \mathbf{H^{n+\frac{1}{2}}} = \epsilon_0 \epsilon_\infty \frac{\mathbf{E^{n+1}} - \mathbf{E^n}}{\mathbf{\Delta t}} + \frac{\mathbf{P_{tot}^{n+1}} - \mathbf{P_{tot}^n}}{\mathbf{\Delta t}} + \sigma \frac{\mathbf{E^{n+1}} + \mathbf{E^n}}{\mathbf{2}}
$$

which can be rewritten as

$$
2\Delta t \nabla \wedge \mathbf{H^{n+\frac{1}{2}}} = \mathbf{E^{n+1}}(\mathbf{2\epsilon_0\epsilon_\infty} + \sigma\mathbf{\Delta t}) - \mathbf{E^n}(\mathbf{2\epsilon_0\epsilon_\infty} - \sigma\mathbf{\Delta t}) + \mathbf{2}(\mathbf{P_{tot}^{n+1}} - \mathbf{P_{tot}^n}). \tag{6.3}
$$

The algorithm models the dispersion effects through the polarisations. In state-of-the-art research, computer resources like memory are much less restrictive issues than the accuracy

of the results. Thus, the algorithm is presented using $LADE^+$ and $DADE^+$ (although it works equally well with $LADE$ and $DADE$). The update equations for the Lorentz-polarisation (5.23) and for the Drude-polarisation (5.4) are used again. The polarisation current from Raman-scattering is given by equation (5.52). In order to avoid the Newton-iteration needed to solve the non-linear equation (6.3) for $\mathbf{E^{n+1}}$ when the Kerr-effect is present, a new variable has to be introduced in equation (5.48):

$$I^n \doteq |\mathbf{E^n}|^\mathbf{2}.$$

The updating of I^n will be described later in this section. Failed attempts as well as other possible solutions to this 'Kerr-problem' will be discussed at the end of this section. The polarisation-term in equation (6.3) can now be written as

$$\mathbf{P_{tot}^{n+1}} - \mathbf{P_{tot}^n} = \sum_{l=1}^{L}(\mathbf{P_l^{n+1}} - \mathbf{P_l^n}) + \sum_{d=1}^{D}(\mathbf{P_d^{n+1}} - \mathbf{P_d^n})$$
$$+ \alpha\epsilon_0\chi_0^3(I^{n+1}\mathbf{E^{n+1}} - I^\mathbf{n}\mathbf{E^n}) + \epsilon_\mathbf{0}(\mathbf{R^{n+1}}\mathbf{E^{n+1}} - \mathbf{R^n}\mathbf{E^n}) \qquad (6.4)$$

Inserting the polarisation equation (6.4) into (6.3) gives the final expression of the ADM^+ algorithm:

$$\mathbf{E^{n+1}} = \mathbf{C_1}\mathbf{E^n} + \mathbf{C_2}\nabla \wedge \mathbf{H^{n+\frac{1}{2}}} + \mathbf{C_3}\left[\sum_{l=1}^{L}(\mathbf{P_l^{n+1}} - \mathbf{P_l^n}) + \sum_{d=1}^{D}(\mathbf{P_d^{n+1}} - \mathbf{P_d^n})\right] \qquad (6.5)$$

with update coefficients

$$C_1 = \frac{2\epsilon_0\epsilon_\infty - \sigma\Delta t + 2\epsilon_0 R^n + 2\alpha\epsilon_0\chi_0^3 I^n}{2\epsilon_0\epsilon_\infty + \sigma\Delta t + 2\epsilon_0 R^{n+1} + 2\alpha\epsilon_0\chi_0^3 I^{n+1}}$$
$$C_2 = \frac{2\Delta t}{2\epsilon_0\epsilon_\infty + \sigma\Delta t + 2\epsilon_0 R^{n+1} + 2\alpha\epsilon_0\chi_0^3 I^{n+1}}$$
$$C_3 = \frac{2}{2\epsilon_0\epsilon_\infty + \sigma\Delta t + 2\epsilon_0 R^{n+1} + 2\alpha\epsilon_0\chi_0^3 I^{n+1}}$$

The big advantage of the update equation (6.5) is that each polarisation contribution can be switched on and off separately. This means that if there is only Lorentz-dispersion, then ADM^+ reduces to $LADE^+$. If there is only Drude-dispersion, then ADM^+ reduces to $DADE^+$. While the modelling of Raman-scattering requires almost no additional computation, the Kerr-effect is an expensive extension. In order to update the Kerr-effect coefficient I, a fixed point iteration has to be performed because a Newton-iteration does not converge in this particular problem. The equation for this fixed point iteration is

$$I_{k+1}^{n+1} = \mathbf{E_k^{n+1}} \cdot \mathbf{E_k^{n+1}}$$
$$= \left(C_1^k\mathbf{E^n} + \mathbf{C_2^k}\nabla \wedge \mathbf{H^{n+\frac{1}{2}}} + \mathbf{C_3^k}\left[\sum_{l=1}^{L}(\mathbf{P_l^{n+1}} - \mathbf{P_l^n}) + \sum_{d=1}^{D}(\mathbf{P_d^{n+1}} - \mathbf{P_d^n})\right]\right)$$
$$\cdot \left(C_1^k\mathbf{E^n} + \mathbf{C_2^k}\nabla \wedge \mathbf{H^{n+\frac{1}{2}}} + \mathbf{C_3^k}\left[\sum_{l=1}^{L}(\mathbf{P_l^{n+1}} - \mathbf{P_l^n}) + \sum_{d=1}^{D}(\mathbf{P_d^{n+1}} - \mathbf{P_d^n})\right]\right) \qquad (6.6)$$

where

$$C_1^k = \frac{2\epsilon_0\epsilon_\infty - \sigma\Delta t + 2\epsilon_0 R^n + 2\alpha\epsilon_0\chi_0^3 I^n}{2\epsilon_0\epsilon_\infty + \sigma\Delta t + 2\epsilon_0 R^{n+1} + 2\alpha\epsilon_0\chi_0^3 I_k^{n+1}}$$

$$C_2^k = \frac{2\Delta t}{2\epsilon_0\epsilon_\infty + \sigma\Delta t + 2\epsilon_0 R^{n+1} + 2\alpha\epsilon_0\chi_0^3 I_k^{n+1}}$$

$$C_3^k = \frac{2}{2\epsilon_0\epsilon_\infty + \sigma\Delta t + 2\epsilon_0 R^{n+1} + 2\alpha\epsilon_0\chi_0^3 I_k^{n+1}}$$

are updated at each iteration. In the one dimensional case it was found empirically that 16 iterations were required to obtain sufficient accuracy. With every iteration the result's accuracy was increased by one order of magnitude. With 16 iterations machine accuracy is reached. The fixed point iteration, which requires the most computational time of the updating process, can be skipped when there is no Kerr-effect needed such that computational speed is retained.

Remarks on the 'Kerr-Problem' In the following discussion it is assumed that the Newton-iteration method presented by [2] ($GVADE$ algorithm, section 5.5) would converge to the correct result if enough iterations are performed. The result of the one dimensional algorithm after 4 iterations was hence used as reference-accuracy for other, faster possible solutions of a medium with linear Lorentz-dispersion, Raman-scattering and Kerr-effect. These other attempts to avoid the expensive Newton-iteration shall be described here briefly. The Newton-iteration reached after 4 iterations machine accuracy. This computation time is therefore set as reference time of the problem. The terms fast and very fast will mean in this context that the computational time was 2, or at least 4 times shorter respectively, while slow and very slow will mean that computational time is 2 times and at least 4 times longer respectively. The accuracy of these other approaches is described as the maximum difference of the field amplitudes between the new approach and the reference occurred during 1000 time steps which is normalized to the maximum field amplitude inside the medium of the reference method.

- Using I^n instead of I^{n+1}: the algorithm is stable, very fast and requires no new variable to be stored. The result deviates by an order of 30%.

- Linear extrapolation from $\mathbf{E^{n-1}}$ and $\mathbf{E^n}$ to $\mathbf{E^{n+1}} \rightarrow \mathbf{I^{n+1}}$: the algorithm is stable, very fast and requires no new variable to be stored. The result deviates by an order of 10%.

- Linear extrapolation from $\mathbf{E^{n-2}}, \mathbf{E^{n-1}}$ and $\mathbf{E^n}$ to $\mathbf{E^{n+1}} \rightarrow \mathbf{I^{n+1}}$ where the two differences are weighted differently, e.g. 2-1-weighted:

$$\mathbf{E^{n+1}} = \left(\mathbf{E^n} + (2\mathbf{E^n} - 2\mathbf{E^{n-1}} + 1\mathbf{E^{n-1}} - \mathbf{E^{n-2}})/3\right)$$

This algorithm is stable, very fast and requires no new variable to be stored. The result deviates by an order of 3%.

- Performing quadratic interpolation between $\mathbf{E^{n-2}}$,$\mathbf{E^{n-1}}$ and $\mathbf{E^n}$ which is then used as extrapolation to $\mathbf{E^{n+1}} \rightarrow \mathbf{I^{n+1}}$. This algorithm is stable, very slow and requires no new variable to be stored. The result deviates by an order of 3%.

- Including spatially neighbouring field information (instead of only temporal extrapolation) and performing then interpolations is slower and has an accuracy of approximately 5%.

- Using the constitutive equations which relate $\mathbf{E}$ to $\mathbf{H}$ via impedance turns the algorithm unstable.

- Using a doubled Yee-grid such that both $\mathbf{E}$ and $\mathbf{H}$ are present in every grid-point and then approximating $\mathbf{E_1^{n+1}}$ by $\mathbf{E_2^{n+\frac{1}{2}}}$ and vice-versa is only 'stable' for very few time steps.

- Using a Lorentz-oscillator and solve it like the Raman-scattering. By setting the Lorentz-pole far enough away from the traversing pulse frequencies, then the polarisation contribution can be considered to be constant (this is what is done in fact to derive the Kerr-effect physically). Going far above the resonance (which is physically incorrect), the algorithm is stable and very fast, but the results are completely wrong. Going far below resonance, the time-step Δt has to be decreased by some orders of magnitude (in order to obtain stability) such that the simulation time and space is increased tremendously. This approach is hence not practicable.

- Using Newton-iteration instead of simple fixed point iteration in order to reduce the number of iterations is not practicable, as the problem is badly conditioned for Newton-iteration (and as an inverse matrix has to be computed for every iteration).

- Using other means to find the roots of equation (6.6) (a third-order polynomial in I^{n+1}) like the ones provided by Matlab is very slow and the automatic choice of the correct root for the update is difficult (which is true for any root-finding approach to this problem).

The linear extrapolation approaches presented above as well as other variations of extrapolations (3-1 weighting, linear least square fitting, etc.) resulted in very fast computation but no smaller deviation than 3% was reached and as a consequence, these approaches were considered as not working.

6.2 Arbitrary Dispersive Permeability

As it was pointed out in section 3 about the double negative materials, it might be desirable to allow the magnetic permeability not only to be unequal to 1 but even dispersive. Furthermore it might proof useful to include the nonlinear Kerr-effect as suggested by [13]. It was shown in section 3 that dispersion relations for the magnetic permeability $\mu(\omega)$ are given by a Lorentz-oscillator. As it is imaginable, that also other dispersive behaviours of $\mu(\omega)$ are possible, a Lorentz- and Drude-behaviour will be implemented in ADM^+. This approach also allows to analyse the wave propagation in a left-handed band of a Lorentz-Lorentz or a Drude-Drude-material instead of a finely tuned Lorentz-Drude-model. The derivation of the update equations is completely analogous to the derivation performed in the previous section for the electric permittivity and.

First, consider Faraday's law

$$\nabla \wedge \mathbf{E} = -\frac{\partial \mathbf{B}}{\partial t} + \mathbf{j_m}$$
$$= \mu_0 \mu_\infty \frac{\partial \mathbf{H}}{\partial t} + \frac{\partial \mathbf{M_{tot}}}{\partial t} + \sigma^* \mathbf{H} \tag{6.7}$$

where $\mathbf{j_m} = \sigma^* \mathbf{H}$ are possible magnetic currents. For a medium with L Lorentz-poles, D Drude-poles and Kerr-effect the total magnetisation $\mathbf{M_{tot}}$ can be written as

$$\mathbf{M_{tot}} = \sum_{l=1}^{L} \mathbf{M_l} + \sum_{d=1}^{D} \mathbf{M_d} + \mathbf{M_{Kerr}} \tag{6.8}$$

Performing the steps described in the previous section at length, and introducing the new variable $K^{n-\frac{1}{2}} \doteq |H^{n-\frac{1}{2}}|^2$ to describe the Kerr-effect-like response of the permeability, the update equations for the magnetic field is given by

$$\mathbf{H^{n+\frac{1}{2}}} = \mathbf{C_1}\mathbf{H^{n-\frac{1}{2}}} - \mathbf{C_2}\nabla \wedge \mathbf{E^n} + \mathbf{C_3}\left[\sum_{l=1}^{L}(\mathbf{M_l^{n+\frac{1}{2}}} - \mathbf{M_l^{n-\frac{1}{2}}}) + \sum_{d=1}^{D}(\mathbf{M_d^{n+\frac{1}{2}}} - \mathbf{M_d^{n-\frac{1}{2}}})\right] \tag{6.9}$$

with update coefficients

$$C_1 = \frac{2\mu_0\mu_\infty - \sigma^*\Delta t + 2\chi_M^3\mu_0 K^{n-\frac{1}{2}}}{2\mu_0\mu_\infty + \sigma^*\Delta t + 2\chi_M^3\mu_0 K^{n+\frac{1}{2}}}$$
$$C_2 = \frac{2\Delta t}{2\mu_0\mu_\infty + \sigma^*\Delta t + 2\chi_M^3\mu_0 K^{n+\frac{1}{2}}}$$
$$C_3 = \frac{2}{2\mu_0\mu_\infty + \sigma^*\Delta t + 2\chi_M^3\mu_0 K^{n+\frac{1}{2}}},$$

where χ_M^3 is the strength of the Kerr-effect-like response of the permeability. The magnetisations are updated with the same equations as the polarisations just by replacing $\mathbf{P}$ by $\mathbf{M}$ and $\epsilon_{0/\infty}$ by $\mu_{0/\infty}$: Lorentz-magnetisation is updated via equation (5.23), Drude-magnetisation is updated via equation (5.4) and Kerr-magnetisation is updated via a fixed point iteration similar to the one given by equation (6.6).

6.3 The Arbitrary Dispersive Material Algorithm

Now that all update equations were derived, the complete ADM^+ algorithm can be formulated as follows:

1. Magnetisation update is performed (in arbitrary order):

   - Lorentz update: $\mathbf{M_l^{n-\frac{1}{2}}} \to \mathbf{M_l^{n+\frac{1}{2}}}$ via equation (5.23) (replace μ, $\mathbf{M}$)
   - Drude update: $\mathbf{M_d^{n-\frac{1}{2}}} \to \mathbf{M_d^{n+\frac{1}{2}}}$ via equation (5.4) (replace μ, $\mathbf{M}$)
   - Kerr update: $K^{n-\frac{1}{2}} \to K^{n+\frac{1}{2}}$ via fixed point iteration (6.6) (replace μ, $\mathbf{M}$)

2. Magnetic field $\mathbf{H^{n-\frac{1}{2}}}$ is updated via equation (6.9) to $\mathbf{H^{n+\frac{1}{2}}}$

3. Polarisation update is performed (in arbitrary order):

   - Lorentz update: $\mathbf{P_l^n} \to \mathbf{P_l^{n+1}}$ via equation (5.23)
   - Drude update: $\mathbf{P_d^n} \to \mathbf{P_d^{n+1}}$ via equation (5.4)
   - Raman update: $R^n \to R^{n+1}$ via equation (5.51)
   - Kerr update: $I^n \to I^{n+1}$ via fixed point iteration (6.6)

4. Electric field $\mathbf{E^n}$ is updated via equation (6.5) to $\mathbf{E^{n+1}}$

The accuracy of the proposed algorithm was tested by comparing the results obtained with ADM^+ with those of [2] and they were found to be in good agreement. Thus, ADM^+ is considered to be accurate.

6.3.1 Remarks on the ADM-Algorithm

The ADM^+ algorithm is highly modular. Any dispersive effect can be removed or added if desired without changing the algorithm's update equations. ADM^+ can be split such that different contributions to update equations are computed separately. For example the standard Yee-algorithm part can be computed on the acceleration hardware *Acceleware* while the polarization terms are computed on the local machine. This is one of the big advantages ADM^+ has compared to the approach in [2].

It is straightforward to add also Debye-dispersion to ADM^+ using the formulas derived in section 5.3. As it is unphysical to have all three linear dispersions present in one medium, Debye-dispersion is not covered by this thesis. To model Debye-dispersion, it is recommended to use the formulation with polarisation currents $\mathbf{J}$ instead of the polarisations $\mathbf{P}$ because the latter is only stable above resonance, i.e. $\omega > 2\pi/\tau$ while the former is stable in any regime. On the other hand, it is not known which formalism yields more accurate results when both are stable.

The solution of a material exhibiting the Kerr-effect presented in [2] ($GVADE$ using Newton-iteration) and the one presented in this thesis (using fixed point iteration) are so far the only known solutions to the problem in three dimensions. Besides that the ADM^+ algorithm is faster than the one presented by [2] it is also expected to show higher accuracy as ADM^+ incorporates $LADE^+$ and $DADE^+$ while [2] uses $LADE$.

7 Stability of the ADM-Algorithm

7.1 Fixed Point Iteration Convergence

The convergence of the fixed point iteration which is needed to solve for the Kerr-effect is proven by using Banach's fixed point theorem [33].

To reduce notational complexity, the convergence of the fixed point iteration will be shown for the one-dimensional case. For brevity, equation (6.6) can be written as

$$I^{n+1} = \frac{a^2}{(b + cI^{n+1})^2} = f(I^{n+1}) \tag{7.1}$$

where

$$a = (\epsilon_\infty - \frac{\sigma \Delta t}{2\epsilon_0} + R^n + \alpha \chi^3 I^n) E^n + \frac{\Delta t}{\epsilon_0} \nabla \wedge H^{n+\frac{1}{2}} + \frac{1}{\epsilon_0} \Delta P$$

$$b = \epsilon_\infty + \frac{\sigma \Delta t}{2\epsilon_0} + R^{n+1}$$

$$c = \alpha \chi^3.$$

The term ΔP stands for the polarisation contributions by Lorentz- and Drude-poles. For simplicity, the third-order susceptibility χ^3 shall be written without the susceptibility index,i.e. $\chi = \chi^3$, for the rest of this section. The fixed point theorem is then applied to $f(I^{n+1})$. To this end, it has to be shown that the first derivation of $f(I)$ is limited $\forall I^{n+1}$ at least within an interval D:

$$f'(I^{n+1}) = \frac{-2a^2 c}{(b + cI^{n+1})^3}. \tag{7.2}$$

Apparently, the supremum of $|f'(I^{n+1})|$ is given where $I^{n+1} = 0$ and is

$$S = \sup_{I^{n+1} \in D} |f'(I^{n+1})| = \frac{2a^2 c}{b^3} \tag{7.3}$$

(the infimum is given where $I^{n+1} = \infty$ and is equal to 0). However, one has to be very careful with these remarks because the 'constant' a is in fact dependent on I^n as $\sqrt{I^n} = E^n$. Thus, in reality, the course of $a(I^n)$ has to be considered. As it will be shown later on, this dependence on I^n of a results in a condition which limits the fixed point convergence to an electric amplitude interval, i.e. $D = [0, I^n_{max}]$. It has now to be shown that the above supremum S is smaller than 1 such that $f(I^{n+1})$ is Lipschitz-continuous with a Lipschitz-constant $L \leq 1$ and consequently, $f(I^{n+1})$ is a contraction on D and the fixed point iteration will be convergent $\forall I^{n+1} \in D$. The condition for $f(I^{n+1})$ to be a contraction on the interval D can be written as

$$a^2 c \leq \frac{b^3}{2}. \tag{7.4}$$

Two extremal cases for the Kerr-effect can be considered:

1. $\alpha = 0$: no Kerr-effect, only Raman-scattering is present $\Rightarrow c = 0$ and equation (7.4) is always satisfied (but the fixed point iteration would not be required)

2. $\alpha = 1$: only Kerr-effect is present, no Raman-scattering $\Rightarrow R^n = 0 \ \forall n$

For the second case, the inequality (7.4) has to be further analysed. A first remark can be made on the conductivity σ. The following holds: $\sigma \Delta t \geq 0$ (as long as $\sigma \geq 0$; otherwise, one has to argue that $\sigma \Delta$ is small compared to all other present terms in (7.4)). Thus, the inequality (7.4) will be strengthened by the presence of conductivity, as b will be increased and a decreased. Thus, in order to further reduce the complexity, set $\sigma = 0$.

Due to the nature of continuity of the used equations, respectively because the temporal and spatial grid have accurately high resolutions, the terms containing spatial and temporal derivations can be considered small compared with the term proportional to the electric field and can hence be neglected. Thus, the contraction condition (7.4) can now be written as

$$[(\epsilon_\infty + \chi I^n)E^n]^2 \chi I^n \leq \frac{\epsilon_\infty^3}{2}.$$

In one dimension $I^n = (E^n)^2$ and the final expression is given by

$$E^{n4}(1 + 2\chi E^n + \chi^2 E^{n2}) \leq \frac{\epsilon_\infty^3}{2\chi}. \tag{7.5}$$

Apparently, the amplitude of the electric field E^n has to be limited to an upper value which is determined by the amplitude of the third-order susceptibility χ in order to assure convergence of the fixed point iteration. In this context it is interesting to note, that also the Newton-iteration used by [2] becomes unstable for field amplitudes larger than E_{max}^n. Equality in (7.5) is reached at E_{max}^n, such that the convergence interval $D = [0, I_{max}^n = E_{max}^{n2}]$. E_{max}^n can be raised to any desired value by decreasing χ. But for a specific material where χ is fixed, only a limited range of intensities can by applied. Furthermore, one has to be aware that the above result is an upper limit which lies too high because some terms were neglected. As a consequence, it is recommended to choose amplitudes that are enough below the above limit.

An example of the definition of the convergence interval D can be seen in figure (21). The upper interval-limit is given where the lines cross each other. The figure shows the limits for three different values of χ (solid: $\chi = 0.1$, dotted: $\chi = 0.2$, dashed: $\chi = 1$) where $\epsilon_\infty = 1$. It can be seen, that the smaller the value of χ the larger is the upper limit for the field amplitude.
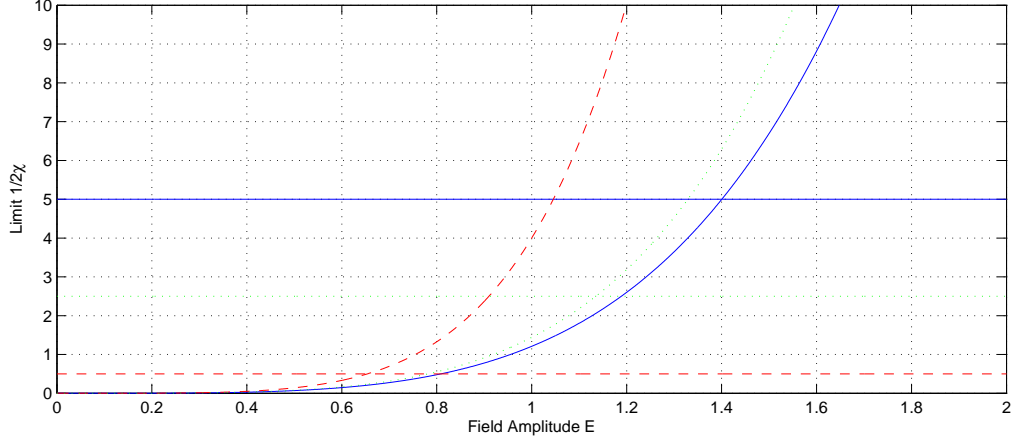
Figure 21: The graph shows how the convergence interval D is limited by the electric field amplitude. It shows the upper interval-limits (where the lines cross each other) for three different values of χ (solid: $\chi = 0.1$, dotted: $\chi = 0.2$, dashed: $\chi = 1$) where $\epsilon_\infty = 1$.

7.2 Dispersion-Relation and Phase-Error

It has to be emphasised again, that ADM^+ incorporates $LADE^+$ and $DADE^+$. The stability of these two algorithms is hence important to be understood. The dispersion relation, which yields information on the algorithm's stability, and the phase error, which gives information on the algorithm's accuracy, of ADM^+ were already derived in section 5.1.3 about the stability of $DADE^+$ and 5.2.3 about the stability of $LADE^+$. The influence on the stability of the Kerr-effect and the Raman-scattering were discussed in section 5.5.4.

As a rule of thumb, one might say that which ever polarisation contributions, i.e. Drude-, Lorentz-polarisation, Kerr-effect or Raman-scattering, are required in the simulation, the more restrictive conditions of either of these has to be satisfied at least to ensure stability. But this must not always be the case, because as soon as different effects are combined, the stability conditions are altered. It is though not possible to give analytical solutions which answer the question of stability and accuracy as it was possible for cases with one single effect. It is though possible to solve the resulting equations numerically which will be done next.

After the derivations in the previous sections about algorithm stability, it should be no surprise that the dispersion relation can be written in the most general case as

$$\Omega^2 \epsilon_{num} \mu_{num} = \mathbf{K} \cdot \mathbf{K} c^2 \tag{7.6}$$

where ϵ_{num} and μ_{num} are the numerical permittivity and numerical permeability respectively.

Assuming a medium with a permeability μ with one Drude- (with pole frequency $\omega_{d\mu}$, damping factor $\delta_{d\mu}$), one Lorentz-pole (with pole frequency $\omega_{l\mu}$, damping factor $\delta_{l\mu}$ and amplitude $\Delta\mu$) and Kerr-effect (with amplitude χ_μ^3) and with a permittivity ϵ incorporating one Drude- (with pole frequency $\omega_{d\epsilon}$, damping factor $\delta_{d\epsilon}$), one Lorentz-pole (with pole

frequency $\omega_{l\epsilon}$, damping factor $\delta_{l\epsilon}$ and amplitude $(1-\alpha)\chi_\epsilon^3$), Kerr-effect (with amplitude $\alpha\chi_\epsilon^3$) and Raman-scattering (with pole frequency ω_R, damping factor δ_R). For ADM^+ algorithm, numerical permittivity and numerical permeability are given by

$$\epsilon_{num} = \epsilon_\infty + \alpha\chi_\epsilon^3|\mathbf{E}|^2 + \frac{\mathbf{\Delta}\epsilon\omega_{\mathbf{l\epsilon}}^2}{\omega_{\mathbf{l\epsilon}}^2 - \mathbf{\Omega^2} - \mathbf{2i\Omega}\delta_{\mathbf{l\epsilon}}} - \frac{\omega_{\mathbf{d\epsilon}}^2}{\mathbf{\Omega^2} + \mathbf{i\Omega}\delta_{\mathbf{d\epsilon}}} + \frac{(\mathbf{1}-\alpha)\chi_\epsilon^{\mathbf{3}}\omega_{\mathbf{R}}^2|\mathbf{E}|^2}{\omega_{\mathbf{R}}^2 - \mathbf{\Omega^2} + \mathbf{2}\delta_{\mathbf{R}}\mathbf{i\Omega}}, \quad (7.7)$$

$$\mu_{num} = \mu_\infty + \chi_\mu^3|\mathbf{H}|^2 + \frac{\mathbf{\Delta}\mu\omega_{\mathbf{l\mu}}^2}{\omega_{\mathbf{l\mu}}^2 - \mathbf{\Omega^2} - \mathbf{2i\Omega}\delta_{\mathbf{l\mu}}} - \frac{\omega_{\mathbf{d\mu}}^2}{\mathbf{\Omega^2} + \mathbf{i\Omega}\delta_{\mathbf{d\mu}}}. \quad (7.8)$$

Inserting these expressions into the numerical dispersion relation (7.6) and solving it for the numerical phase vector k yields

$$k = \frac{2}{\Delta}\arcsin\left[\frac{\sqrt{\epsilon_{num}\mu_{num}}}{S}\sin\left(\frac{\pi S}{N_\lambda}\right)\right]. \quad (7.9)$$

This equation can be solved numerically. A sufficiently large sampling of the traversing wave ensures that the wave will not aphysically decay and that the phase velocity is accurate. This fact is shown in figure 22 where the real (solid) and imaginary dashed) parts of the phase velocity $v = \omega/k$ are shown as functions of the grid sampling number N_λ. For N_λ large enough, the imaginary part vanishes and the numerical phase velocity approaches the physical phase velocity. The phase velocity is though somewhat different than the one shown in figure 14. While the imaginary part is there always larger than 0, it is here always below 0. This behaviour seems to be attributed to the presence of the damping terms in the Drude-dispersions. However, one has to be aware that the exact course of numerical phase velocity as a function of the grid sampling number depends on the used values and can hence show some deviation of the curve shown in figure 22. As it can be seen from figure 23, a higher grid sampling number increases the accuracy. This behaviour is, as expected, independent of the chosen values for the problem. Thus, the numerical phase velocity approaches the physical phase velocity to an arbitrary accuracy as long as the grid sampling number is large enough. All the results derived here were observed and thus verified in a one-dimensional simulation in Matlab.

Due to the high complexity of the numerical permittivity and permeability of an arbitrary dispersive material it is not possible to derive a simple stability condition like the ones found for $DADE^+$ and $LADE^+$. The dispersion relation (7.6) has to be solved for Ω but as it is a high-order odd polynomial in Ω this is not possible. It seems that this is not even feasible numerically. It is though possible to derive stability conditions, i.e. a condition for the time-step Δt such that the algorithm is stable, for special cases of the ADM^+ such as Drude-Drude- (μ and ϵ follow a single Drude-pole with no absorption, i.e. $\delta = 0$), Drude-Lorentz-materials, Lorentz-Lorentz-materials. These special solutions can give at least an indication of the stability conditions valid for the ADM^+-algorithm.
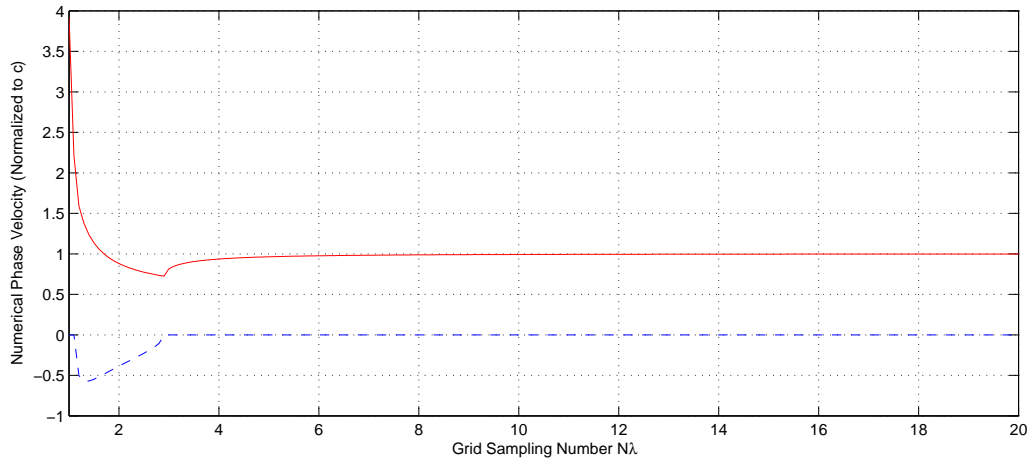
Figure 22: The real (solid line) and imaginary (dashed line) parts of the phase velocity $v = \omega/k$ are shown as functions of the grid sampling number N_λ of ADM^+. For N_λ larger than ~ 2.5 (given by (5.18)), the imaginary part vanishes and the numerical phase velocity approaches the physical phase velocity.
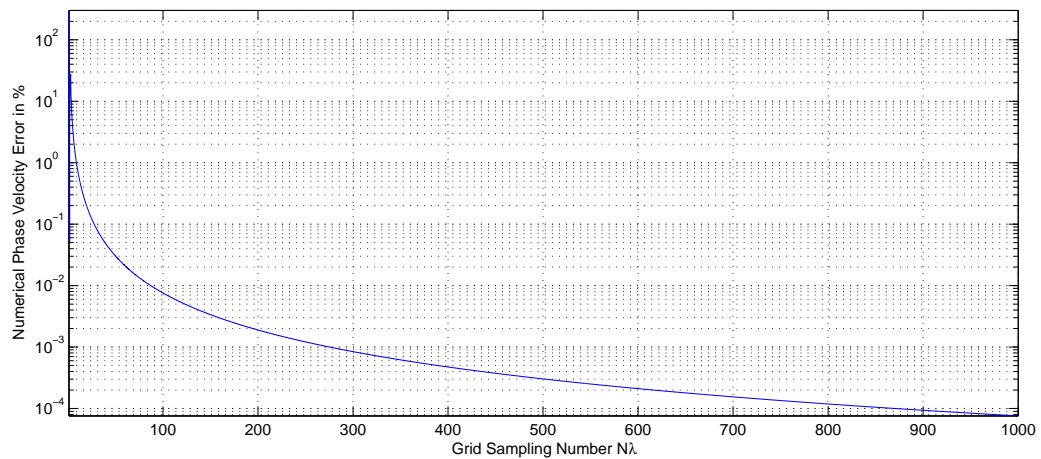

Figure 23: The plot shows the percental error of the phase velocity as a function of the grid sampling number N_λ of ADM^+. A higher N_λ ensures a higher accuracy.

8 Results of ADM^+

The ADM^+ algorithm incorporates $DADE^+$ and $LADE^+$. The effects of a light-pulse traversing a dispersive medium with either a single Drude- or a single Lorentz-pole was already discussed and illustrated in the sections 5.1.5 and 5.2.5. Due to the ability of ADM^+ to model linear dispersion as well as non-linear Raman-scattering and Kerr-effect, it is possible to simulate non-linear materials, and especially non-linear double negative materials. The effects that occur in such materials are now accessible with ADM^+ and will be discussed and shown in this section. An explanation of the interpretation of the shown results is given in section 5.1.5 in figure 16.

8.1 DNMs with ADM^+

After the extensive discussion of double negative materials in section 3 it is now time to test the predictions. In one dimension it is only possible to test whether a negative phase velocity is present or not, because in order to show negative refraction more than one dimension is needed.

As it was pointed out in section 3, a DNM has permittivity $\epsilon(\omega)$ and a permeability $\mu(\omega)$ that are represented by a Drude- and by a Lorentz-pole respectively. For simplicity, first a DNM where the permittivity $\epsilon(\omega)$ and the permeability $\mu(\omega)$ follow the same single Drude-pole shall be considered. Afterward the same case is considered with Lorentz-poles. These cases will be called Drude-Drude and Lorentz-Lorentz respectively. These cases are particularly simple because such materials have only two transmission bands. In one band both ϵ and μ are positive, in the other band both are negative. Thus, it makes sense to call these bands positive or negative transmission bands. While the positive band is naturally present in all transmissive materials, the negative band is unique to DNMs.

Figure 24 and 25, which is a zoom of the former, show how a light-pulse with carrier frequency ω_0 generated in free space enters a DNM consisting of a Drude-Drude material with $\epsilon(\omega_0) = \mu(\omega_0) = -1$. It can be readily seen that the development of the phase fronts which is seen as lines inside the light-pulse undergoes a drastic transition when passing across the DNM boundary. The angle of the development of the phase fronts changes sign when entering the DNM which is equivalent to the change of sign in the phase-velocity. While the phase velocity undergoes a sign-change, the group-velocity remains positive but it is strongly slowed down due to the dispersion from $\epsilon(\omega)$ and $\mu(\omega)$. Furthermore it can be seen that the light-pulse is broadened and diminished like in a normal dispersive medium.
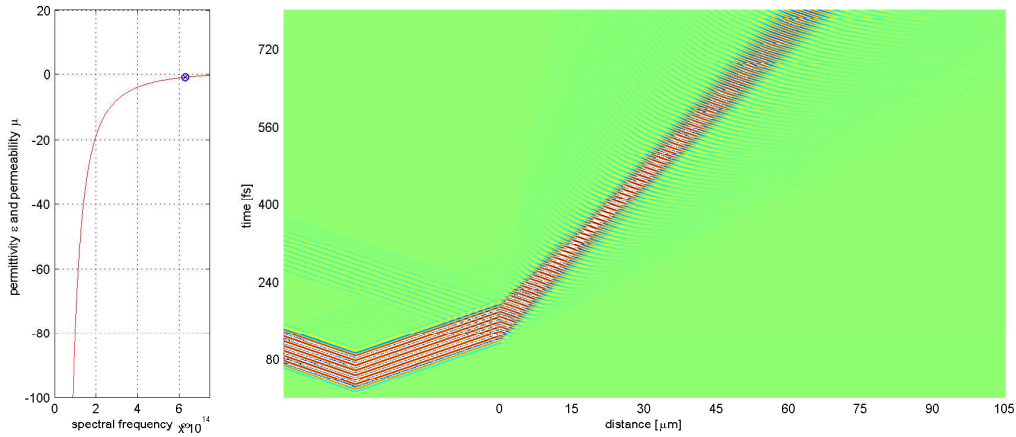
Figure 24: Left: Course of $\epsilon(\omega)$ and $\mu(\omega)$ and indication of location of ω_0. Right: A light-pulse with carrier frequency ω_0 generated in free space enters at 0 a DNM consisting of a Drude-Drude material with $\epsilon(\omega_0) = \mu(\omega_0) = -1$.
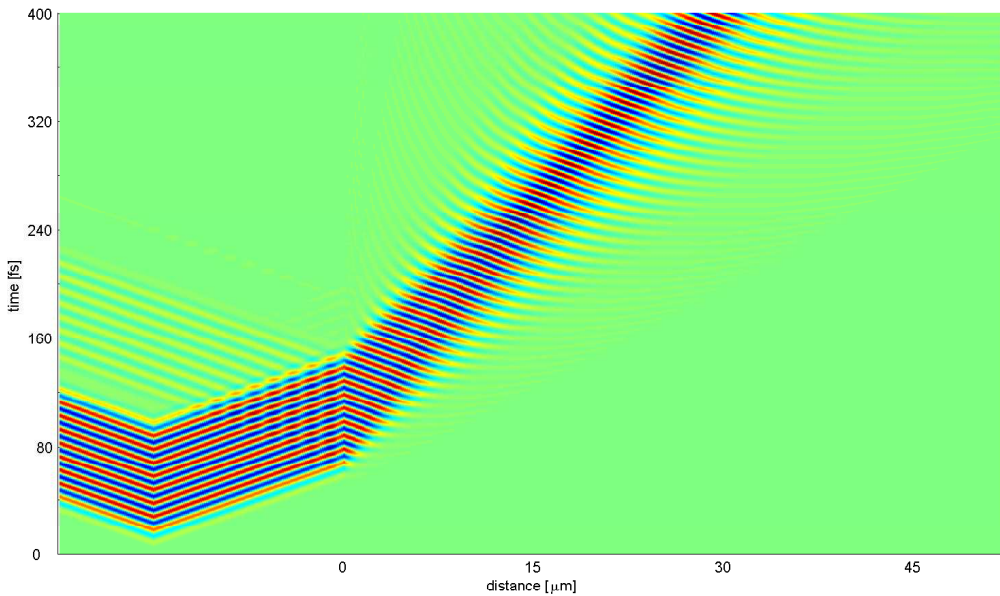

Figure 25: A light-pulse with carrier frequency ω_0 generated in free space enters at 0 a DNM consisting of a Drude-Drude material with $\epsilon(\omega_0) = \mu(\omega_0) = -1$.

Figure 26 shows how a light-pulse with carrier frequency ω_0 generated in free space enters a DNM consisting of a Lorentz-Lorentz material with $\epsilon(\omega_0) = \mu(\omega_0) = -1$. Exactly the same phenomenons can be observed as in the Drude-Drude case. The biggest difference is that the group-velocity is altered stronger because a permeability or permittivity that follows a Lorentz-pole varies stronger across a certain frequency interval than one following a Drude-pole.
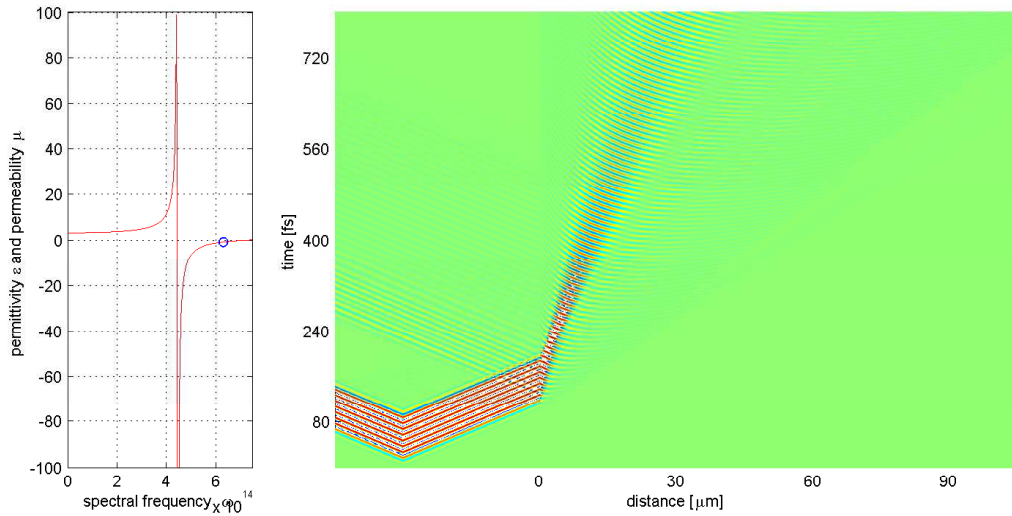
Figure 26: Left: Course of $\epsilon(\omega)$ and $\mu(\omega)$ and indication of location of ω_0. Right: A light-pulse with carrier frequency ω_0 generated in free space enters at 0 a DNM consisting of a Lorentz-Lorentz material with $\epsilon(\omega_0) = \mu(\omega_0) = -1$.

In a next step, a more realistic DNM can be simulated by defining a Drude-Lorentz material. The course of $\epsilon(\omega)$ and $\mu(\omega)$ of the considered material follows a Drude-pole and a Lorentz-pole respectively. Both are shown in figure 27.
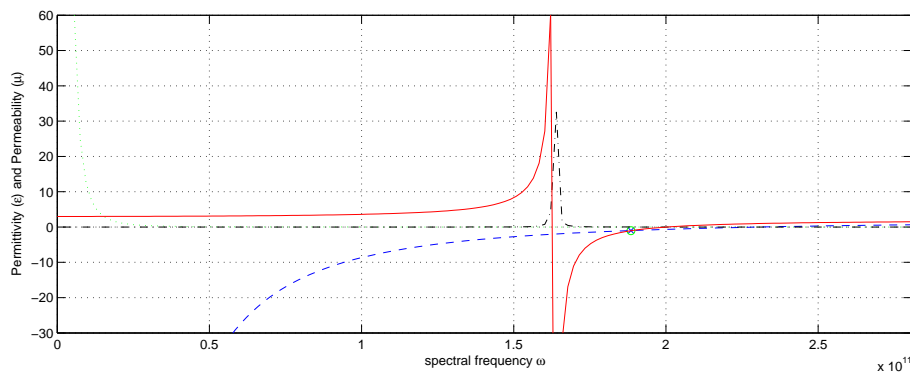

Figure 27: Course of the permittivity $\epsilon(\omega)$ following a Drude-pole where the real part is dashed and the imaginary part dotted and of the permeability $\mu(\omega)$ following a Lorentz-pole where the real part is solid and the imaginary part dash-dot. Such conditions can be found in a realistic DNM. Furthermore the location of the carrier frequency of the light pulse used in figure 29 is indicated.

In such a material several different frequency bands are present which are shown in figure 28. Again, there are the positive and negative pass bands but also two new bands. A light pulse with a carrier frequency ω_0 entering the negative band, i.e. in the DNM regime, is shown in figure 29. In the new bands, $\epsilon(\omega)$ and $\mu(\omega)$ have opposite signs and waves at these specific frequencies cannot travel inside the medium because the refractive index becomes imaginary (see also section I). That is why these bands are also called stop bands. As the waves cannot traverse, respectively, not even enter the material, total reflection of the wave occurs as shown in figure 30.
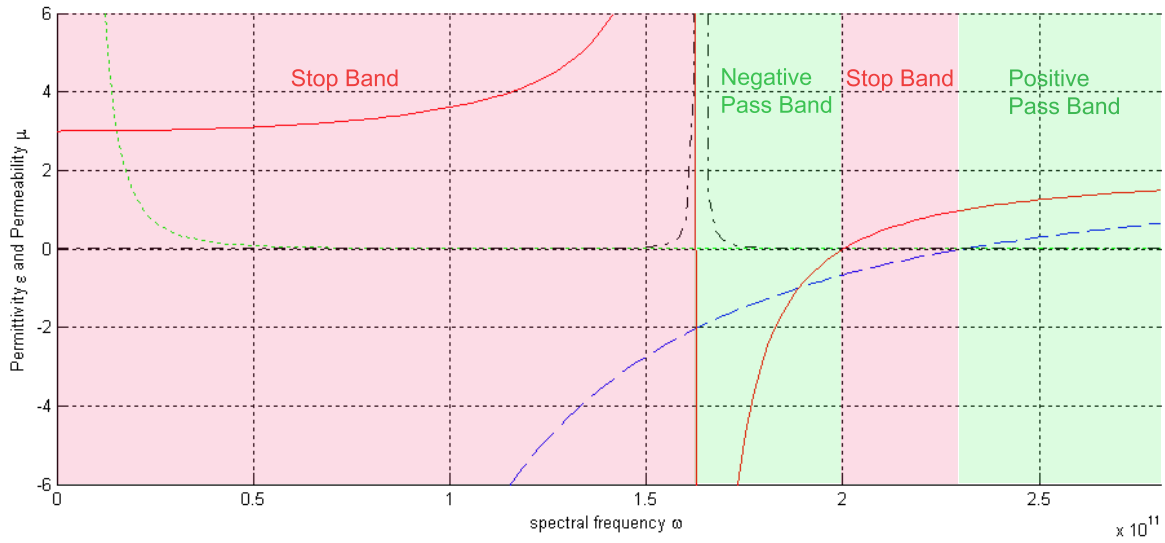

Figure 28: Course of the permittivity $\epsilon(\omega)$ following a Drude-pole where the real part is dashed and the imaginary part dotted and of the permeability $\mu(\omega)$ following a Lorentz-pole where the real part is solid and the imaginary part dash-dot. Pass-bands are present where $\epsilon(\omega)$ and $\mu(\omega)$ have the same signs, stop bands where $\epsilon(\omega)$ and $\mu(\omega)$ have opposite signs. The narrow pass-band in the middle is where the material is a DNM.
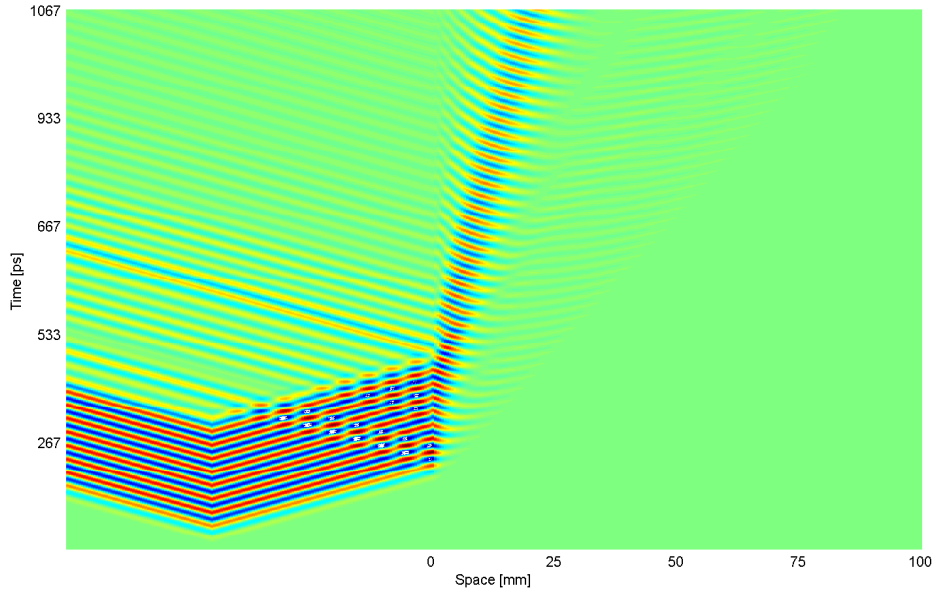
Figure 29: A light-pulse with carrier frequency ω_0 generated in free space enters at 0 a DNM, i.e. ω_0 lies within the negative pass band, consisting of a Drude-Lorentz material with $\epsilon(\omega_0) = \mu(\omega_0) = -1$.
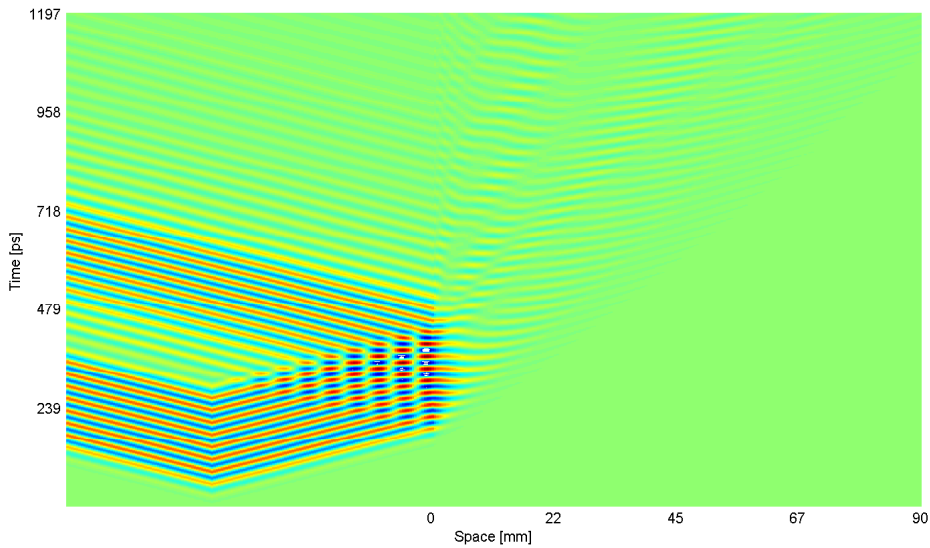

Figure 30: A light-pulse with carrier frequency ω_0 generated in free space enters at 0 a Drude-Lorentz material with $\epsilon(\omega_0) = -0.4$ and $\mu(\omega_0) = 0.4$. ω_0 lies within a stop band and thus, the pulse cannot enter the material and total reflection occurs.

Allowing now that the inspected metamaterial exhibits a self-focusing Kerr-effect it is possible to produce gap solitons as described by [34]. As it has been shown and explained before, in a realistic DNM there exist stop and pass bands. It has been shown that in a stop band no waves are supported. However, if the DNM exhibits a self-focusing Kerr-effect, the transmission properties of the material become intensity dependent. The Kerr-effect is simply an intensity dependent refractive index, more precisely, it can be regarded as an intensity dependent contribution to ϵ_∞. Thus, if the Kerr-effect is positive, i.e. self-focusing, it lifts the entire course of the permittivity $\epsilon(\omega_0)$ or permeability $\mu(\omega_0)$. Assume the same material as the one used before depicted in figure 28 and that the Kerr-effect acts on the permeability. The higher the pulse-intensity the higher is the permittivity lifted by the Kerr-effect and the smaller becomes the stop band. This is shown in figure 31.
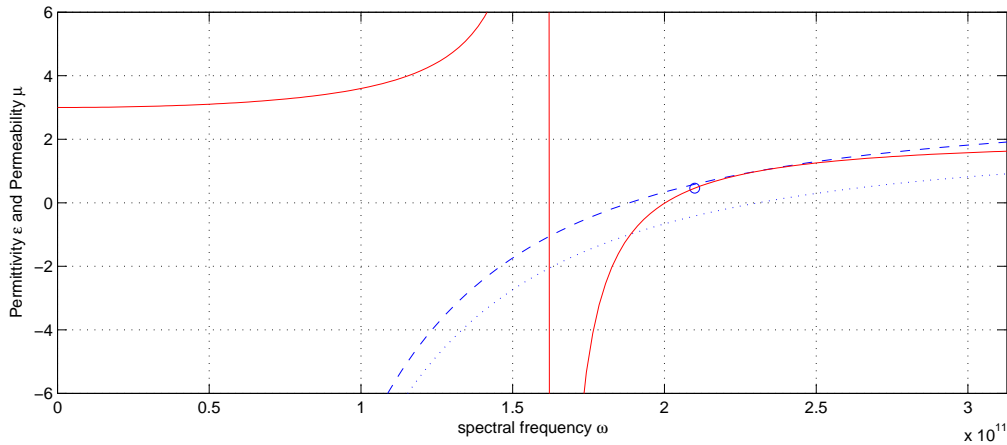

Figure 31: Course of the permittivity $\epsilon(\omega)$ following a Drude-pole where the real part is dotted and of the permeability $\mu(\omega)$ following a Lorentz-pole where the real part is solid. The imaginary parts were omitted. The effect of the Kerr-nonlinearity is to lift the course of the permittivity depending on the beams intensity. This lifting is shown by the dashed line which represents the actual permittivity of the material for a certain intensity.

If the pulse-intensity is high enough then the positive pass band expands at the costs of the stop band and a gap soliton can transverse the DNM. The formation of such a gap soliton is depicted in figure 32 where the same material parameters were used as before, but additionally the Kerr-effect is present.

It is possible to expand the negative pass band in the very same manner by using a defocusing Kerr-effect. But in this case, the pulse gets broadened and diminished by dispersion and Kerr-effect such that only few of the initial intensity is transmitted.
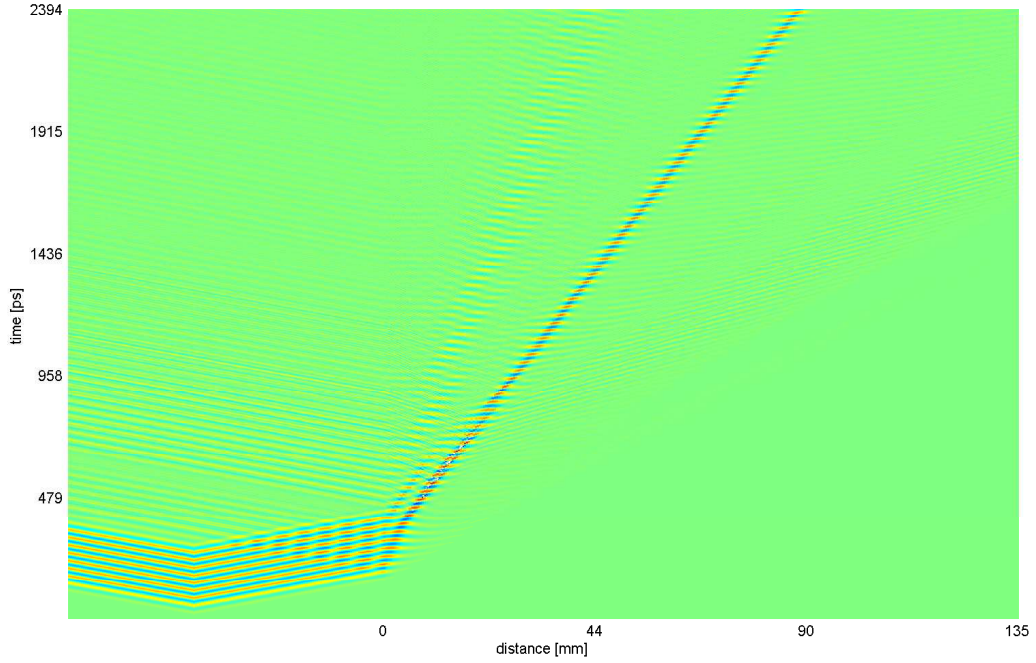
Figure 32: A light-pulse with carrier frequency ω_0 generated in free space enters at 0 a Drude-Lorentz material with $\epsilon(\omega_0) = -0.4$ and $\mu(\omega_0) = 0.4$ and with self-focusing Kerr-effect. ω_0 lies within a stop band which is reduced by the Kerr-effect. Hence, a gap soliton can form and traverse the stop band.

8.2 Solitons with ADM^+

A light-pulse entering a material suffers pulse-broadening due to linear dispersion because every frequency that supports the light-pulse travels at a slightly different velocity. As an example, pulse-broadening due to a single Lorentz-pole is shown in figure 33.
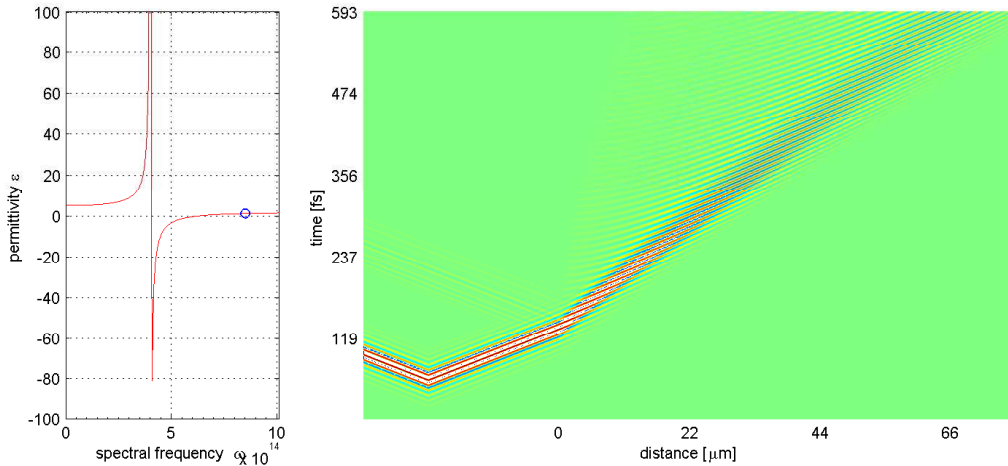

Figure 33: Left: Permittivity of the material with a single Lorentz-pole the position of the carrier-frequency of the pulse. Right: A light-pulse is formed outside a material with a permittivity given by the left figure. The pulse enters the material at 0 and gets broadened afterward.

Allowing non-linear effects such as the Kerr-effect results in self-focusing of the pulse. If the broadening due to dispersion and the focusing due to Kerr-effect are well balanced, then the pulse retains its shape while traversing the material which is shown in figure 34. Because of the high complexity of soliton formation, a more thorough discussion of solitons would be far beyond the scope of this work. The material used in figure 34 has exactly the same Lorentz-pole like the one used in figure 33 but it also exhibits Kerr-effect and Raman-scattering.

Figure 35 shows snapshots of the soliton shown in figure 34 at different times. Additionally, a so-called precursor-pulse which proceeds the soliton is observed. This precursor-pulse is in the previous image not visible because its amplitude is too small. These results reproduce those of [35].

Summary of Validation   The new algorithm ADM^+ has been validated in various one-dimensional simulations. It has been shown, that ADM^+ allows to simulate linear dispersive materials such as DNMs correctly as pulse broadening as well as negative phase velocities have been observed and occurred as expected. Also non-linear effects were tested and it has been shown that ADM^+ is able to simulate solitons and that it reproduces the results of [35]. Furthermore, ADM^+ allowed to test the predictions of [34] who described
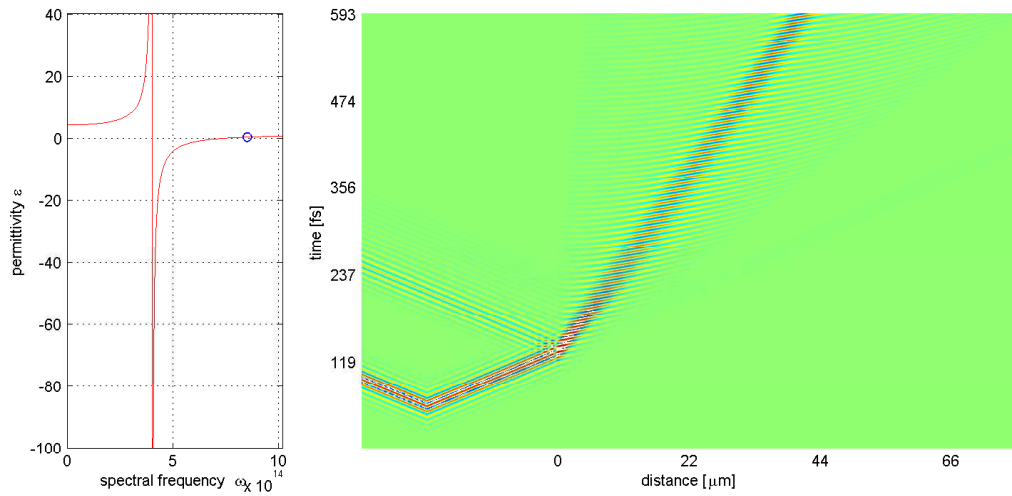
Figure 34: Left: Permittivity of the material with a single Lorentz-pole and the position of the carrier-frequency of the pulse. Right: A light-pulse is formed outside a material with a permittivity given by the left figure. The pulse enters the material at 0 and forms a pulse which does not change its shape, i.e. a soliton is formed.
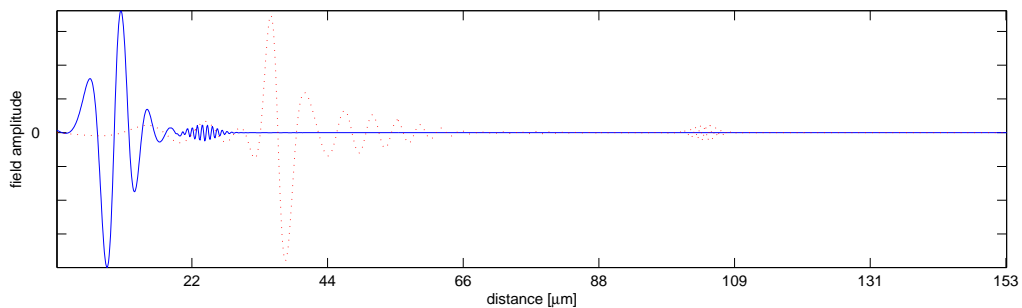

Figure 35: Snapshots of the soliton's electric field shown in figure 34 at different times. Additionally a so-called precursor-pulse which proceeds the soliton is observed.

the new phenomenon of gap-solitons which occur in non-linear DNMs. This phenomenon could be confirmed.

9 Conclusions

The following tasks have been accomplished:

- Discussion of physical material-models and electromagnetic wave interaction with these materials (parts I)

- Derivation of ADE FDTD algorithms for material models of one non-trivial dispersion relation (part II) and their stability conditions

- Derivation of a new algorithm and its stability conditions (part III)

- Simulations of DNMs (sections 3.6 and 8)

After the analysis of several algorithms of which each allowed to solve Maxwell's equations in a material that exhibits only one particular dispersion relation or intensity dependence of the refractive index, it was found that it is possible to cover all of these effects with the novel and efficient ADM algorithm. The novel approach bases on the introductino of the intensity as a new variable which allows to update the contribution from the Kerr-effect separately. The update equation for the intensity can be solved by a fixed-point iteration. Stability conditions of ADM and a convergence criteria for the fixed-point iteration were derived analytically.

ADM has the following advantages:

- Material-Models: ADM^+ covers linear Drude- and Lorentz-polarisation, non-linear Kerr-effect and Raman-scattering (section 6).

- Speed: ADM^+ is faster than any other similar algorithm (section 6).

- Modularity: each polarisation contribution can be computed separately facilitating parallelisation (section 6).

- Stability: Stability conditions for ADM^+ were derived analytically for some special cases while for the most general case of ADM^+ it is not feasible. Furthermore, a convergence criteria of the fixed-point iteration was derived by applying Banach's fixed-point theorem (section 7).

Its high computational speed and complete modularity are its main advantages compared with other similar algorithms. The proposed algorithm allows to simulate electromagnetic wave propagation in a material with an arbitrary number of Drude- and Lorentz-poles in its dispersion relation and, additionally, non-linear Kerr-effect and Raman-scattering.

The new algorithm allows in particular to simulate double negative materials. Different effects such as negative phase velocity and gap-solitons that occur in such DNMs were demonstrated in one-dimensional tests of the algorithm.

10 Outlook

It is intended to implement the full three-dimensional ADM-algorithm into Semcad X [1] opening all new fields of applications. Among these are very active, fast growing research fields such as non-linear DNMs and the formation of so-called light-bullets, three-dimensional solitons.

Future developments of the ADM^+ could include further non-linear third-order effects such as sum- and difference-frequency generation, two-photon absorption and Cotton-Mouton effect. Non-linear intensity-dependencies of the refractive index are imaginable as discussed in [36]. If anisotropic materials are included, non-linear second-order effects such as sum- and difference-frequency generation, Pockels-effect, Faraday-effect and parametric amplification. Furthermore it would be possible to implement more exact (less general) models of metamaterial components such as the split ring resonators (as described by [23]).

List of Abbreviations

Abbreviation	Denotation
ADE	Auxiliary Differential Equation
ADeb	Debye Auxiliary Differential Equation Algorithm derived using polarisation currents
ADeb$^+$	Deby Auxiliary Differential Equation Algorithm derived using polarisation
ADM	Arbitrary Dispersive Material Algorithm
ADM$^+$	Arbitrary Dispersive Material Algorithm incorporating *DADE$^+$* and *LADE$^+$*
DADE	Drude Auxiliary Differential Equation Algorithm derived using polarisation currents
DADE$^+$	Drude Auxiliary Differential Equation Algorithm derived using polarisation
DNM	Double Negative Material
FDTD	Finite-Difference Time-Domain
GVADE	General Vector Auxiliary Differential Equation Algorithm derived by [2]
LADE	Lorentz Auxiliary Differential Equation Algorithm derived using polarisation currents
LADE$^+$	Lorentz Auxiliary Differential Equation Algorithm derived using polarisation
LHM	Left-Handed Material
NIR	Near Infrared
NUV	Near Ultraviolet
SRR	Split-Ring Resonator

Acknowledgments

I would like to thank *Prof. W. Fichtner* from the Integrated Systems Laboratory (IIS) at the Swiss Federal Institute of Technology Zurich (ETH) to accept me as Diploma-student.

My thanks go also to *Prof. N. Kuster* who allowed me to write my Diploma-thesis at IT'IS Foundation.

Special Thanks go to my supervisors *Dr. N. Chavannes* and *S. Schild* for guiding me through my Diploma-thesis, their great support and advice.

Furthermore, I would like to express my gratitude to *Dr. N. Felber* for his administrative support.

Big thanks are sent to the *IT'IS and SPEAG team members* not only for their support and advice but also for accepting me as part of their great team.

Final thanks go out to it my family who supported me throughout my time at ETH. Many thanks go to *Corinne* who cheered up my life during my time at ETH.

References

[1] Schmidt & Partner Engeneering AG. Semcad-x reference manual. 2006.

[2] J. H. Greene and A. Taflove. General vector auxiliary differential equation finite-difference time-domain method for nonlinear optics. *Optics Express*, 14:8305–8310, 2006.

[3] A. Taflove and S. C. Hagness. Computational electrodynamics, the finite-difference time-domain method. *Artech House*, 2005.

[4] H. Ibach and H. Lüth. Festkörperphysik. *Springer*, 2001.

[5] R. W. Boyd. Nonlinear optics. *Academic Press*, 2003.

[6] R. M. Hill and L. A. Dissado. Debye and non-debye relaxation. *Journal of Physics C: Solid State Physics*, 18:3829–3836, 1985.

[7] K. J. Blow and D. Wood. Theoretical description of transient stimulated raman scattering in optical fibers. *Journal of Quantum Electronics*, 25:2665–3673, 1989.

[8] V. G. Veselago. The electrodynamics of substances with simultaneously negative values of epsilon and mu. *Soviet Physics Uspekhi*, 10:509–514, 1968.

[9] A. D. Boardman et al. Negative refraction in perspective. *Electromagnetics*, 25, 2005.

[10] J. B. Pendry et al. Extremely low frequency plasmons in metallic mesostructures. *Physical Review Letters*, 76, 1996.

[11] J. B. Pendry et al. Magnetism from conductors and enhanced nonlinear phenomena. *IEEE Transactions on Microwave Theory and Techniques*, 47:2075–2084, 1999.

[12] A. A. Zharov et al. Nonlinear properties of left-handed metamaterials. *Physical Review Letters*, 91:037401–1 – 037401–4, 2003.

[13] I. Kourakis and P. K. Shukla. Nonlinear propagation of electromagnetic waves in negative-refraction-index composite materials. *Physical Review E*, 72:016626–1 – 016626–5, 2005.

[14] R. A. Shelby et al. Experimental verification of a negative index of refraction. *SCIENCE*, 292:77–79, 2001.

[15] C. Enkirch et al. Magnetic metamaterials at telecommunication and visible frequencies. *Physical Review Letters*, 95:203901–1 – 203901–4, 2005.

[16] J. B. Brock et al. Focusing inside negative index materials. *Applied Physics Letters*, 85:2472–2474, 2004.

[17] D. Schurig et al. Metamaterial electromagnetic cloak at microwave frequencies. *SCIENCE*, 314:977–980, 2006.

[18] T. M. Grzegorczyk et al. Properties of left-handed metamaterials: Transmission, backward phase, negative refraction and focusing. *IEEE Transactions on Microwave Theory and Techniques*, 53:2956–2967, 2005.

[19] Z. G. Dong et al. Numerical simulations of negative-index refraction in wedge-shaped metamaterials. *Physical Review E*, 72:016607–1 – 016607–5, 2005.

[20] S. Foteinopoulou et al. Refraction in media with a negative refractive index. *Physical Review Letters*, 90:107402–1 – 107402–4, 2003.

[21] C. D. Moss et al. Numerical studies of left handed metamaterials. *Progress in Electromagnetics Research*, 35:315–334, 2002.

[22] J-Y. Lee et al. Effective medium approach of left-handed material using a disperisve fdtd method. *IEEE Transactions on Magnetics*, 40:1484–1487, 2005.

[23] I. V. Shadrivov et al. Nonlinear left-handed metamaterials. *Radio Science*, 40:RS3S90–1 – RS3S90–10, 2005.

[24] N. A. Zharova et al. Nonlinear transmission and spatiotemporal solitons in metamaterials with negative refraction. *Physical Review E*, 72:016607–1 – 016607–5, 2005.

[25] P. F. Loschialpo et al. Optical properties of an ideal homogeneous causal left-handed material slab. *Physical Review E*, 70:036605–1 – 036605–11, 2004.

[26] M. K. Kärkkäinen. Numerical study of wave propagation in uniaxially anisotropic lorentzian backward-wave slabs. *Physical Review E*, 68:026602–2 – 026602–6, 2003.

[27] M. Ahmadlou et al. Negative refraction and focusing analysis in a left-handed material slab and realization with a 3d photonic crystal. *Journal of Optics A: Pure and Applied Optics*, 8:199–204, 2006.

[28] J. B. Pendry. Negative refraction makes a perfect lens. *Physical Review Letters*, 85:3966–3969, 2000.

[29] J. B. Pendry and S. A. Ramakrishna. Near-field lenses in two dimensions. *Journal of Physics: Condensed Matter*, 14:8463–8479, 2002.

[30] K. S. Yee. Numerical solution of initial boundary value problems involving maxwell's equations in isotropic media. *IEEE Transactions on Antennas and Propagation*, 14:302–307, 1966.

[31] J. L. Young. Propagtion in linear dispersive media: Finite difference time-domain methodologies. *IEEE Transactions on Antennas and Propagation*, 43:422–426, 1995.

[32] M. Okoniewski and E. Okoniewska. Drude dispersion in ade fdtd revisited. *Electronics Letters*, 42, 2006.

[33] K. Königsberger. Analysis 2. *Springer*, 2000.

[34] S. Longhi. Gap solitons in nonlinear self-focusing metamaterials. *Quantum Electronics and Laser Conference (QELS)*, pages 1405–1407, 2005.

[35] M. Fuji et al. High-order fdtd and auxiliary differential equation formulation of optical pulse propagation in 2-d kerr and raman nonlinear dispersive media. *IEEE Journal of Quantum Electronics*, 40:175–182, 2004.

[36] R. H. Enns and D. E. Edmundson. Guide to fabricating bistable-soliton-supporting media. *Physical Review A*, 47:4524–4527, 1993.